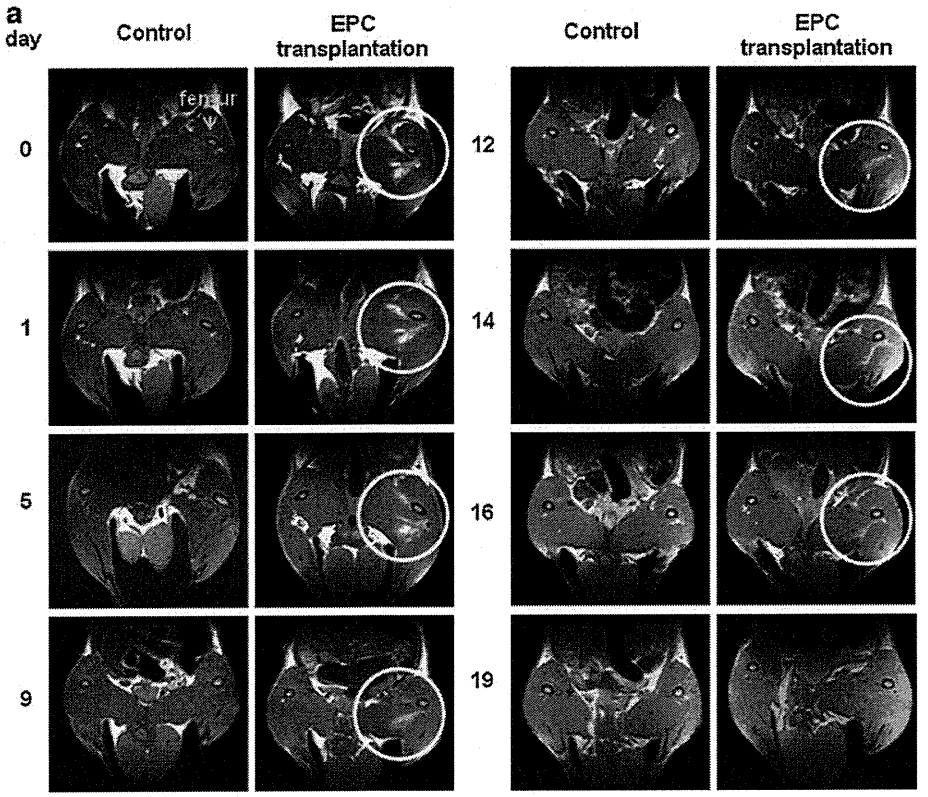

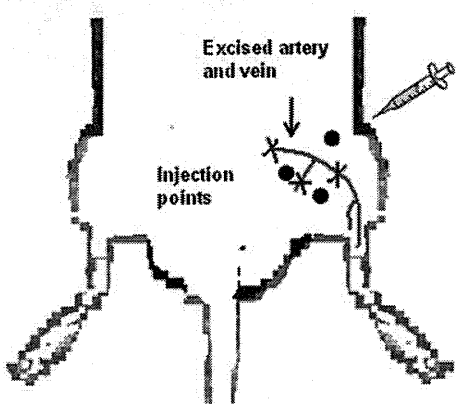

FIG. 5. MR images of Dex-DOTA-Gd^{3+}-labeled EPCs (2×10^7) after intramuscular injection in ischemic limb rat models. **(a)** Bolheal® was used as a scaffold. T_1-weighted images were acquired at days 0, 1, 5, 9, 12, 14, 16, and 19 after transplantation by using a 1.5-T compact MR imaging system. Sequence, spin echo; coronal slice, 1 mm; TR, 2000 ms; TE, 9 ms; and image acquisition matrix, 128×256. **(b)** Rat position in the MRI. Color images available online at www.liebertonline.com/tea

ages obtained *in vivo* by using a 1.5-*T* animal MRI system within 20 days after transplantation. Cells could be clearly detected in the muscles and were observed to migrate for at least 16 days until the cells totally vanished at day 19. A rat was then sacrificed 6 days after transplantation, and the zone that appeared in the MR image was excised. The MR images in Figure 6a show that the cells are located in the adductor muscle. Frozen section slides revealed the presence of Qtracker 655-labeled EPCs in the ischemic area. During the development of the method for tracking EPCs *in vivo*, we observed that $5–6.3\times10^6$ labeled cells diluted in 50 μL of Bolheal were necessary to achieve cell imaging at least 14 days after transplantation.

Immunohistochemical staining for von Willebrand factor and (AP) of the removed muscles at 35 days revealed the presence of numerous capillary endothelial cells in the rats implanted with Dex-DOTA-Gd^{3+}-labeled EPCs (Fig. 7a); capillary/muscle fiber ratios for this rat group markedly increased (two-fold, $p<0.001$; Fig. 7b) relative to the ratio for the ischemic control group. There were no significant differences in capillary density between the ischemic control and the normal limb ($p<0.05$; Fig. 7b). This blood flow recovery by the EPC transplantation suggests that our cell labeling system based on Dex-DOTA-Gd3+ electroporation does not affect cell viability, cell growth, or stem cell functions.

Discussion

BM-derived EPCs were successfully labeled with Dex-DOTA-Gd^{3+} by electroporation at 0.12 pg of Gd per cell. This extent of labeling is significantly lower than 12 pg of iron oxide/cell,[16] but is nonetheless sufficient to achieve the signal enhancement required to provide good contrast in the body during MRI measurements. Several investigations on magnetic labeling of cells for MRI tracking *in vitro* and *in vivo* have shown that iron oxide nanoparticles are suitable for imaging stem cells.[10,12,39] Nevertheless, more recent reports have called into question its use as a contrast agent, because of false-positive MRI signals, which lead to inconsistencies between a persistently positive MRI signal and histologically labeled cells.[16,2,40–42]

Commonly used Gd complex contrast agents such as DOTA-Gd^{3+} and Magnevist exhibit relatively slow relaxation times in comparison to Dex-DOTA-Gd^{3+}. This is because these contrast agents are simpler and low-molecular weight structures and need higher doses of contrast agent to accomplish the same resolution. The incorporation of DOTA-Gd^{3+} into dextran is likely to have caused an increase in the relaxation time due to a steric limitation imposed on the rotational movement of the polymer, which leads to an increase in the rotational correlation coefficient.[43,44] In addition, DOTA-Gd conjugated to a biocompatible dextran carrier and the free Dex-DOTA-Gd^{3+} are expected to be rapidly cleared from the body and to have few interactions with the cell membrane because of their high solubility.

Our results demonstrate that Dex-DOTA-Gd^{3+} achieves intracellular labeling through electroporation, which is an essential condition for labeling cells. A membrane modified with a polymer will interfere with cell-cell interactions during the recruitment of cells in the mechanism of angiogenesis. A polymer in the cell membrane can be easily detached and may be taken up and transferred to other cells *in vivo*. The fluorescence intensity of the cell lysis solution suggests that Dex-DOTA-Gd^{3+} remains stable in the EPCs for at least 25 days (Fig. 4c). A decrease in the fluorescence intensity indicates that the polymer has leaked out of cells during culture or that cells are dying, but no significant change in the fluorescence intensity has been demonstrated in the labeled EPCs. In addition, the cells showed a normal proliferation rate (during 10 days)[45] after Dex-DOTA-Gd^{3+} labeling by electroporation.

An additional cell proliferation activity and viability analysis was performed by using the WST-1 assay system. The results demonstrated that EPCs were not affected in the first 10 days after labeling by electroporation with Dex-DOTA-Gd^{3+} as a MRI contrast agent. No statistically significant differences were found between the proliferation of labeled and nonlabeled EPCs. After 10 days, the EPCs stopped proliferating and the quantity of cells remained stable. The viability claims are backed up with evidence for the first 10 days.

In vivo MR images indicate that the Dex-DOTA-Gd^{3+}-labeled EPCs are perfectly detectable and that the fate of the cells can be followed within 16 days after transplantation with a cell density of $5–6\times10^6$ cells/0.05 mL (Fig. 5). Labeled cells totally faded after 19 days. This is likely due to cell bio-distribution during cell migration, which is probably caused by cytochemical attraction of EPCs via incorporation into newly formed vessels and may also be influenced by the release of pro-angiogenic factors in a paracrine manner.[28,46–48] Moreover, it is likely that cellular proliferation occurs *in vivo*. This would reduce the concentration of the polymer inside the EPC cytoplasm and cause low contrast in the limb. The proliferation rate of the labeled cells *in vitro* indicated that after 10 days, the cells increased in number by three-folds, and the fluorescence intensity remained stable. This indicates that the concentration of Dex-DOTA-Gd^{3+} remained constant but the concentration per cell might be reduced by three-folds. Analogous to the *in vitro* results shown in Figure 2b, if the image contrast of 6×10^6 cells is reduced by three-folds, the signal intensity should be similar to the signal provided by 2×10^6 cells. If this intensity reduction is assumed *in vivo*, the 6.3×10^6 labeled cells transplanted into the ischemic limb 10 days after proliferation could then be tracked, because the Dex-DOTA-Gd^{3+} still has the capacity to produce a signal. At day 14 after implantation of labeled cells, the concentration of Dex-DOTA-Gd^{3+} underwent a four-fold reduction, which is the limit of the signal intensity provided by this contrast agent.

A rat was sacrificed 6 days after implantation of labeled cells. Muscles were carefully excised with particular attention to the location where MR images showed labeled cells. The presence of Qtracker 655-labeled EPCs localized in the neovascular zones of the ischemic limb ensures that MRI signals correspond to signals generated by the labeled cells (Fig. 6a). In addition, the number of macrophages found in the muscles (Fig. 6b) was insignificant, but was related to the obtained MR images or cells. This ensures that in contrast to cells loaded with iron oxide, the Dex-DOTA-Gd^{3+}-labeled EPCs have not been subjected to endocytosis by the macrophages and are reliable for tracking of labeled cells over a long period.

Preliminary *in vivo* data suggest that Dex-DOTA-Gd^{3+}-labeled cells were incorporated into sites of neovascularization and arranged into the capillary network. Direct local transplantation of labeled cells into the ischemic limb was found to quantitatively augment the capillary density in the ischemic limb *in vivo*.

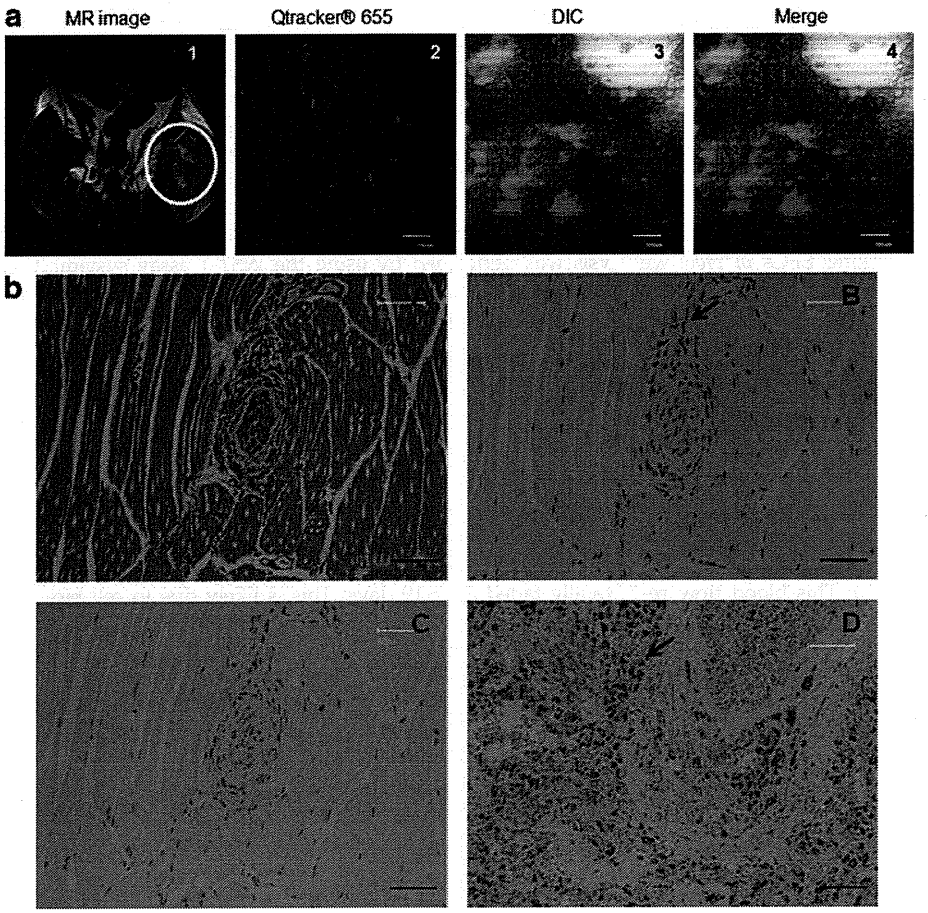

FIG. 6. Identification of transplanted EPCs in the ischemic limb. **(a)** Six days after transplantation of Dex-DOTA-Gd^{3+}-labeled and Qtracker® cell 655-labeled EPCs, a rat was sacrificed to demonstrate that MR images of the cells inside the muscle match the EPCs transplanted in the ischemic limb. (1)The MR image corresponds to the rat before sacrifice. The circle shows the location of labeled cells in the ischemic limb. (2) Frozen section of tissues dissected specifically in the area wherein the MR image indicated staining with Qtracker cell 655. (3) Differential interference contrast, and (4) Merge image. **(b)** Immunohistochemical analysis for identification of the macrophages in the transplanted area: hematoxylin and eosin staining **(A)**, CD68 **(B)**, CD68 negative control, without reaction with the secondary antibody **(C)**, and CD68 positive control from rat spleen **(D)**. The arrow indicates a positive macrophage. Scale bar = 50 μm. Color images available online at www.liebertonline.com/tea

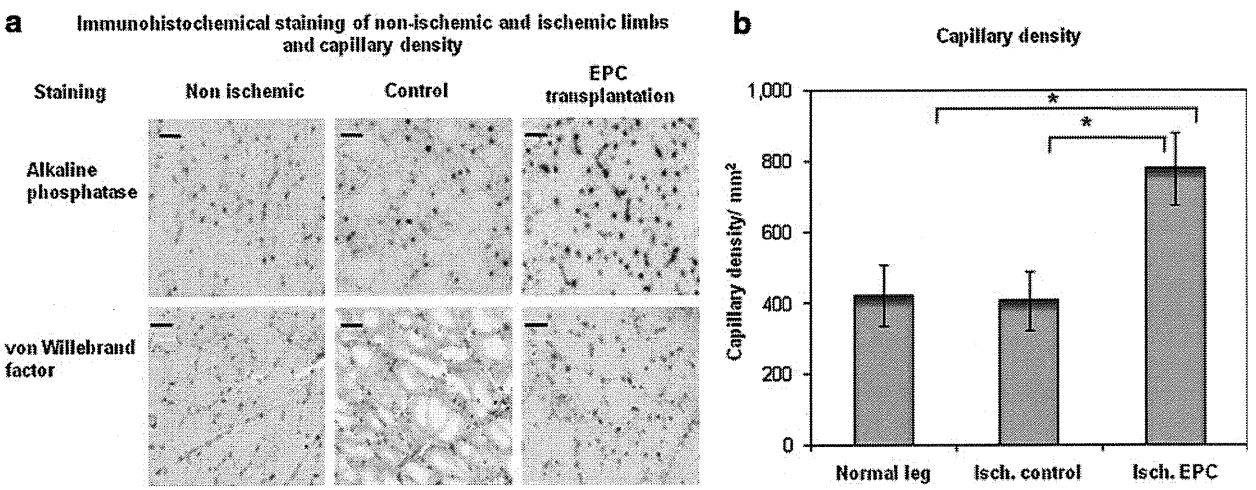

FIG. 7. Immunohistochemical staining of the nonischemic and ischemic limbs and determination of capillary density Immunohistochemical staining for AP and vWF staining indicates viable endothelial cells. Five fields from two muscle samples from each animal ($n = 9$) were randomly selected. **(a)** Capillary density is shown as the ratio of capillary to muscle fiber from frozen sections prepared from the muscles of ischemic limbs 35 days after transplantation of Dex-DOTA-Gd^{3+}-labeled EPCs and ischemic controls. $^*p < 0.05$ versus normal limb and ischemic control **(b)**. AP, alkaline phosphatase; vWF, von Willebrand factor. Color images available online at www.liebertonline.com/tea

Conclusions

The use of MRI for tracking EPCs by using a novel contrast agent in the therapeutic angiogenesis of ischemic limb models would be extremely useful for the anatomical visualization of localization of the transplanted stem cells over a long period. Dex-DOTA-Gd^{3+} as an MRI contrast agent for imaging stem cells *in vivo* has consistently satisfied certain properties such as providing desired MRI contrast properties and *ex vivo* cell labeling before transplantation, generating high-degree and stable intracellular labeling, ensuring biocompatibility without affecting cell viability backed up with evidence for the first 10 days after electroporation, possessing proliferative and healing capacities, and remaining consistently detectable over long periods of time.

Acknowledgments

This work was supported by grant-in-aid from the Ministry of Health, Labour, and Welfare of Japan (Health and Labour Sciences Research Grants, Research on Nanotechnical Medicine) and a Research Grant for Cardiovascular Diseases (18A-2) from the Japan Association for the Advancement of Medical Equipment. The authors thank Jun-ichiro Enmi, Takayuki Ose, Hajime Fukuda, and Akihide Yamamoto for their cooperation.

Disclosure Statement

The authors declare that there are no competing financial interests.

References

1. Rafii, S., Meeus, S., Dias, S., Hattori, K., Heissig, B., Shemelkov, S., Rafii, D., and Lyden, D. Contribution of morrow-derived progenitors to vascular and cardiac regeneration. Cell Devl Biol **13,** 61, 2002.
2. Li, Z., Wu, J.C., Sheikh, A.Y., Kraft, D., Cao, F., Xie, X., Patel, M., Gambhir, S.S., Robbins, R.C., Cooke, J.P., and Wu, J.C. Differentiation, survival, and function of embryonic stem cell derived endothelial cells for ischemic heart disease. Circulation **116,** I-46, 2007.
3. Kondo, K., Shintani, S., Shibata, R., Murakami, H., Murakami, R., Imaizumi, M., Kitagawa, Y., and Murohara, T. Implantation of adipose-derived regenerative cell enhances ischemia induced angiogenesis. Arterioscler Thromb Vasc **B29,** 61, 2009.
4. Murohara T. Autologous adipose tissue as a new source of progenitor cells for therapeutic angiogenesis. J Cardiol **53,** 155, 2009.
5. Cho, S.W., Moon, S.H., Lee, S.H., Kang, S.W., Kim, J., Lim, J.M., Kim, B.S., and Chung, H.H. Improvement of postnatal neovascularization by embryonic stem cell derived endothelial-like cell transplantation in a mouse model of hindlimb ischemia. Circulation **116,** 2409, 2007.
6. Shyu, W.C., Lin, S.Z., Yang, H.I., Tzeng, Y.S., Pang, C.Y., Yen, P.S., and Li, H. Functional recovery of stroke rats induced by granulocyte colony stimulating factor stimulated cells. Circulation **110,** 1847, 2004.
7. Urbich, C., and Dimmeler, S. Endothelial progenitor cells characterization and role in vascular biology. Circ Res **95,** 343, 2004.
8. Urbich, C., Heesechen, C., Aicher, A., Dernbach, E., Zeiher, A.M., and Dimmeler, S. Relevance of monocytic features for neovascularization capacity of circulating endothelial progenitor cells. Circulation **108,** 2511, 2003.
9. Rafii, S., and Lyden, D. Therapeutic stem and progenitor cell transplantation for organ vascularization and regeneration. Nat Med **9,** 702, 2003.
10. Lewin, M., Carlesso, N., Tung, C.H., Tang, T.X., Cory, D., Scadden, D.T. and Weissleder, R. Tat peptide-derivatized magnetic nanoparticles allow *in vivo* tracking and recovery of progenitor cells. Nat Biotechnol **18,** 410, 2000.
11. Hinds, K.A., Hill, J.M., Shapiro, E.M., Laukkanen, M.O., Silva, A.C., Combs, C.A., Varney, T.R., Balaban, R.S., Korestsky, A.P., and Dunbar, C.E. Highly efficient endosomal labeling of progenitor and stem cells with large magnetic particles allows magnetic resonance imaging of single cells. Blood **102,** 867, 2003.
12. Bulte, J.W.M., Douglas, T., Witwer, B., Zhang, S.C., Strable, E., Lewis, B.K., Zywicke, H., Miller, B., Gelderen, P.V., Moskowitz, H., Duncan, I.D., and Frank, J.A. Magnetodendrimers allow endosomal magnetic labeling and *in vivo* tracking of stem cells. Nat Biotechnol **19,** 1141, 2001.
13. Cormode, D.P., Skajaa T., Fayad, Z.A., and Mulder, W.J.M. Nanotechnology in medical imaging probe design and applications. Arterioscler Thromb Vasc Biol **29,** 1, 2009.
14. Wilhelm, C., Bal, L., Smirnov, V., Galy-Fauroux, I., Clement, O., Gazeau, F. and Emmerich, J. Magnetic control of vascular network formation with magnetically labeled endothelial progenitor cells. Biomaterials **28,** 3797, 2007.
15. Daldrup-Link, H.E., Rudelius, M., Piontek, G., Metz, S., Brauer, R., Debus, G., Corot, C., Schlegel, J., Link, T.M., Peschel, C., Rummeny, E., and Oostendorp, R.A. Migration of iron oxide-labeled human hematopoietic progenitor cells in a mouse model: *in vivo* monitoring with 1.5-T MR imaging equipment. Radiology **234,** 197, 2005.
16. Arbab A.S., Frenkel, V., Pandit, S.D., Anderson, S.A., Yocum, G.T., Bur, M., Khuu, H.M., Read, E., and Frank, J.A. Magnetic resonance imaging and confocal microscopy studies of magnetically labeled endotelial progenitor cells tracfficking to sites of tumor angiogenesis. Stem Cells **24,** 671, 2006.
17. Tachibana, Y., Enmi, J.I., Mahara, A., Iida, H., and Yamaoka, T. Design and characterization of a polymeric MRI contrast agent based on PVA for *in vivo* living-cell tracking. Contrast Media Mol Imaging **5,** 1, 2010.
18. Asahara, T., Murohara, T., Sullivan, A., Silver, M., Zee, R.V.D., Li, T., Witzenbichler, B., Schatteman, G., and Isner, J.M. Isolation of putative progenitor endothelial cells for angiogenesis. Science **274,** 964, 1997.
19. Asahara, T., Masuda, H., Takahashi, T., Kalka, C., Pastore, C., Silver, M., Kearne, M., Magner, M., and Isner, J.M. Bone marrow origin of endothelial progenitor cells responsible for postnatal vasculogenesis in physiological and pathological neovascularization. Circ Res **85,** 221, 1999.
20. Shi, Q., Rafii, S., Wu, M.H.D., Wijelath, E.S., Yu, C., Ishida, A., Fujita, Y., Kothari, S., Mohle, R., Sauvage, L.R., Moore, M.A.S., Storb, R.F., and Hammond, W.P. Evidence for circulating bone marrow-derived endothelial cells. Blood **92,** 362, 1998.
21. Kalka, C., Masuda, H., Takahashi, T., Gordon, R., Tepper, O., Gravereaux, E., Pieczek, A., Iwaguro, H., Hayashi, S.I., Isner, J.M., and Asahara, T. Vascular endothelial growth $factor_{165}$ gene transfer augments circulating endothelial progenitor cells in human subjects. Circ Res **86,** 1198, 2000.
22. Iwaguro, H., Yamaguchi, J.I., Kalka, C., Murasawa, S., Masuda, H., Hayashi, S.I., Silver, M., Li, T., Isner, J.M., and Asahara, T. Endothelial progenitor cell vascular endothelial growth factor gene transfer for vascular regeneration. Circulation **105,** 732, 2002.
23. Lyden, D., Hattori, K., Dias, S., Costa, C., Blaikie, P., Butros, L., Chadburn, A., Heissig, B., Marks, W., Witte, L., Wu, Y.,

Hicklin, D., Zhu, Z., Hackett, N.R., Crystal, R.G., Moore, M.A.S., Hajjar, K.A., Manova, K., Benezra, R., and Rafii, S. Impaired recruitment of bone-marrow-derived endothelial and hematopoietic precursor cells blocks tumor angiogenesis and growth. Nat Med **7,** 1194, 2001.
24. Kalka, C., Masuda, H., Takahashi, T., Kalka-Moll, W.M., Silver, M., Kearney, M., LI, T., Isner, J.M., and Asahara, T. Transplantation of *ex vivo* explanted endothelial progenitor cells for therapeutic neovascularization. Proc Natl Acad Sci USA **28,** 3422, 2000.
25. Shintani, S., Murohara, T., Ikeda, H., Ueno, T., Sasaki, K., Duan, J., and Imaizumi, T. Augmentation of postnatal neovascularization with autologous bone marrow transplantation. Circulation **103,** 897, 2001.
26. Cormode, D.P., Skajaa T., Fayad, Z.A., and Mulder, W.J.M. Nanotechnology in medical imaging probe design and applications. Arterioscler Thromb Vasc Biol **29,** 1, 2009.
27. Kamaly, N., Kalber, T., Ahmad, A., Oliver, M.H., So, P.W., Herlihy, A.H., Bell, J.D., Jorgensen, M.R. and Miller, A.D. Bimodal paramagnetic and fluorescent liposomes for cellular and tumor magnetic resonance imaging. Bioconjug Chem **19,** 118, 2008.
28. Takahashi, T., Kalka, C., Masuda, H., Chen, D., Silver, M., Kearney, M., Magner, M., Isner, J.M., and Asahara, T. Ischemia-and cytokine-induced mobilization of bone marrow-derived endothelial progenitor cells for neovascularization. Nat Med **5,** 434, 1999.
29. Murasawa, S., and Asahara, T. Endothelial progenitor cells for vasculogenesis. Physiology **20,** 36, 2005.
30. Kahler, C.M., Wechselberger, J., Hilbe, W., Gschwendtner, A., Colleselli, D., Niederegger, H., Boneberg, E.M., Spizzo, G., Wendel, A., Gunsilius, E., Patsch, J.R., and Hamacher, J. Peripheral infusion of rat bone marrow derived endothelial progenitor cells leads to homing in acute lung injury. J Respir Res **50,** 1465, 2007.
31. Kobayashi, N., Fukushima, H., Takeshima, H., Koguchi, W., Mamada, Y., Hirata, H., Machida, Y., Suzuki, N., Yotsuka, F., Tabei, K., Kobayashi, E., Fukuda, N., and Ishimitsu, T. Am J Hypertens **23,** 1007, 2010.
32. Iwaguro, H., Yamaguchi, J.I., Kalka, C., Murasawa, S., Masuda, H., Hayashi, S.I., Silver, M., Li, T., Isner, J.M., and Asahara, T. Endothelial progenitor cell vascular endothelial growth factor gene transfer for vascular regeneration. Circulation **105,** 732, 2002.
33. Ziada, A.M.A.R., Hudlicka, O., Tyler, K.R., and Wright, A.J.A. The effect of long-term vasodilatation on capillary growth and performance in rabbit heart and skeletal muscle. Cardiovasc Res **18,** 724, 1984.
34. Takeshita, S., Isshiki, T., Mori, H., Tanaka, E., Eto, K., Miyazawa, Y., Tanaka, A., Shinozaki, Y., Hyodo, K., Ando, M., Kubota, M., Tanioka, K., Umetani, K., Ochiai, M., Sato, T., and Miyashita, H. Use of synchrotron radiation microangiography to assess development of small collateral arteries in a rat model of hindlimb ischemia. Circulation **95,** 805, 1997.
35. Yamaoka, T., Tabata, Y., and Ikada, Y. Body distribution of polysaccharides after intravenous administration. Drug Deliv **1,** 75, 1993.
36. Rebizak, R., Schaefer, M., and Dellacherie, E. Polymeric conjugates of Gd^{3+}-diethylenetriaminepentaacetic acid and dextran 1. Synthesis, characterization, and paramagnetic properties. Bioconjug Chem **8,** 605, 1997.
37. De Leon-Rodriguez, L.M., and Kovacs, Z. The synthesis and chelation chemistry of DOTA-peptide conjugates. Bioconjug Chem **19,** 391, 2008.
38. Ladd, D.L., Hollister, R., Peng, X., Wei, D., Wu, G., Delecki, D., Snow, R.A., Toner, J.L. Kellar, K., Eck, J., Desai, V.C., Raymond, G., Kinter, L.B., Desser T.S., and Rubien, D.L. Polymeric gadolinium chelate margetic resonance imaging contrast agents: design, synthesis, and properties. Bioconjug Chem **10,** 361, 1999.
39. Partlow, K.C., Chen, J., Brant, A., Neubauer, A.M., Meyerrose, T.E., Creer, M.H., Caruthers, S.D., Lanza, G.M., and Wickline, S.A. ^{19}F magnetic resonance imaging for stem/progenitor cell tracking with multiple unique perfluorocarbon nanobeacons. FASEB J **21,** 1647, 2007.
40. Amsalem, Y., Mardor, Y., Feinbeg, M.S., Landa, N., Miller, L., Daniels, D., Ocherashvilli, A., Holbova, R., Yosef, O., Barbash, I.M., and Leor, J. Iron-oxide labeling and outcome of transplanted mesenchymal stem cells in the infracted myocardium. Circulation **116,** 38, 2007.
41. Raynal, I., Prigent, P., Peyramaure, S., Najid, A., Rebuzzi, C., and Corot, C. Macrophage endocytosis of superparamagnetic iron oxide nanoparticles. Invest Radiol **39,** 56, 2004.
42. Qiao, H., Zhang, H., Zheng, Y., Ponde, D.E., Shen, D., Gao, F., Bakken, A.B., Schmitz, A., Kung, H.F., Ferrari, V.A., and Zhou, R. Embryonic stem cells grafting in normal and infracted myocardium: serial assessment with MR imaging and PET dual detection. Radiology **3,** 821, 2009.
43. Srinivasachari, S., Fichter, K.M., and Reineke, T.M., Polycationic β-cyclodestrin "click busters": monodisperse and versatile scaffolds for nucleic acid delivery. J Am Chem Soc **130,** 4618, 2008.
44. Mohs, A.M., Wang, X., Goodrich, K.G., Zong, Y., Parker, D.L., and Lu, Z.R. PEG-g-poly(GdDTPA-co-L-cystine): a biodegradable macromolecular blood pool contrast agent for MR imaging. Bioconjug Chem **15,** 1424, 2004.
45. Hur, J., Yoon, C.H., Kim, H.S., Choi, J.H., Kang, H.J., Hwang, K.K., Oh, B.H., Lee, M.M., and Park, Y.B. Characterization of two types of endothelial progenitor cells and their different contribution to neovasculogenesis. Arterioscler Thromb Vasc Biol **24,** 288, 2004.
46. Gill, M., Dias, S., Hattori, K., Rivera, M.L., Hicklin, D., Witte, L., Girardi, L., Yurt, R., Himel, H., and Raffi, S. Vascular trauma induces rapid but transient mobilization of $VEGFR2^+$ $AC133^+$ endothelial precursor cells. Circ Res **88,** 167, 2001.
47. Nissen, N.N., PolverinI, P.J., Koch, A.E., Volin, M.V., Gamelli, R.L., and DiPietro, L.A. Vascular endothelial growth factor mediates angiogenic activity during the proliferative phase of wound healing. Am J Pathol **152,** 1445, 1998.
48. Yamaguchi, J., Kusano, K.F., Masuo, O., Kawamoto, A., Silver, M., Murasawa, S., Bosch-Marce, M., Masuda, H., Losordo, D.W., Isner, J.M., and Asahara, T. Stromal cell-derived factor-1 effects on *ex vivo* expanded endothelial progenitor cell recruitment for ischemic neovascularization. Circulation **107,** 1322, 2003.

Address correspondence to:
Tetsuji Yamaoka, Ph.D.
Departments of Biomedical Engineering
National Cerebral and Cardiovascular Center Research Institute
5-7-1 Fujishiro-dai, Suita
Osaka 565-8565
Japan

E-mail: yamtet@ri.ncvc.go.jp

Received: August 16, 2010
Accepted: April 4, 2011
Online Publication Date: May 18, 2011

Available online at www.sciencedirect.com

SciVerse ScienceDirect

Nuclear Medicine and Biology 38 (2011) 1157–1164

NUCLEAR MEDICINE — AND — BIOLOGY

www.elsevier.com/locate/nucmedbio

Three-dimensional quantitation of regional cerebral blood flow in mice using a high-resolution pinhole SPECT system and ^{123}I-iodoamphetamine☆

Tsutomu Zeniya[a,*], Hiroshi Watabe[b], Takuya Hayashi[c], Takayuki Ose[c], Kazunori Myojin[d], Akihiko Taguchi[d], Akihide Yamamoto[a], Noboru Teramoto[e], Masaru Kanagawa[f], Yoshihiro Yamamichi[f], Hidehiro Iida[a]

[a]*Department of Investigative Radiology, National Cerebral and Cardiovascular Center Research Institute, Suita, Osaka 565-8565, Japan*
[b]*Department of Molecular Imaging in Medicine, Osaka University Graduate School of Medicine, Suita, Osaka 565-0871, Japan*
[c]*Functional Probe Research Laboratory, RIKEN Center for Molecular Imaging Science, Kobe, Hyogo 650-0047, Japan*
[d]*Department of Regenerative Medicine, National Cerebral and Cardiovascular Center Research Institute, Suita, Osaka 565-8565, Japan*
[e]*Department of Surgery (E-1), Division of Cardiovascular Surgery, Osaka University Graduate School of Medicine, Suita, Osaka 565-0871, Japan*
[f]*Research Center, Nihon Medi-physics Co., Ltd., Sodegaura, Chiba 299-0266, Japan*

Received 12 October 2010; received in revised form 28 March 2011; accepted 23 April 2011

Abstract

Introduction: This study is intended to evaluate the feasibility of using a high-resolution pinhole SPECT system and iodine-123-*N*-isopropyl-4-iodoamphetamine (^{123}I-IMP) for three-dimensional (3D) absolute quantitation of regional cerebral blood flow (rCBF) in mice.
Methods: The pinhole SPECT system consists of a rotating stage and a pinhole collimator attached to a clinical gamma camera. The collimator's focal length is 251 mm. Phantom studies were performed to evaluate sensitivity and full-width half-maximum (FWHM) spatial resolution. The aperture-to-object distance was 15 mm. Six mice were studied. Cerebral infarctions were induced by ligating and disconnecting the distal portion of the left middle cerebral artery. Ex vivo SPECT studies were performed using harvested brains and skulls. The CBF volumetric image was computed using the standardized input function.
Results: Excellent spatial resolution of 0.9-mm FWHM and uniform sensitivity throughout the 3D volume were demonstrated in the phantom experiments. The CBF images showed a defect in the infarcted areas and a reduction of CBF values in the infarcted region as compared with the control region.
Conclusions: This study demonstrated the feasibility of the 3D quantitation of rCBF in mice using a high-resolution pinhole SPECT system and ^{123}I-IMP.

Keywords: Pinhole SPECT; ^{123}I-iodoamphetamine; Mouse; Regional cerebral blood flow; High resolution; 3D quantitation

1. Introduction

Imaging of physiological functions (e.g., tissue blood flow or receptor binding potential) in small-animal models of a human disease is invaluable for pharmaceutical development, understanding disease processes and the assessment of new therapies [1]. Such physiological functions can be quantitatively and sensitively evaluated by radionuclide imaging. Unlike autoradiography [2–4], tomographic imaging techniques such as positron emission tomography (PET) or single-photon emission computed tomography (SPECT) allow

☆ This study was partly supported by The Health Labour Science Research Grant from the Ministry of Health, Labour and Welfare (MHLW) of Japan the Budget for Nuclear Research of the Ministry of Education, Culture, Sports, and Technology (MEXT) of Japan; and the Grant-in-Aid for Scientific Research from MEXT of Japan; the Project from Kansai Bureau of Economy, Trade and Industry of Japan.

* Corresponding author. Tel.: +81 6 6833 5012; fax: +81 6 6835 5429.
E-mail address: zeniya@ri.ncvc.go.jp (T. Zeniya).

0969-8051/$ – see front matter © 2011 Elsevier Inc. All rights reserved.
doi:10.1016/j.nucmedbio.2011.04.007

determination of the three-dimensional (3D) distribution of a radiotracer non-invasively. With the use of a 3D image set, the localization of the area of interest can be achieved by superimposing the image onto anatomical images such as magnetic resonance (MR) or X-ray CT images.

Many investigators have imaged rodents using PET or SPECT [5,6]. Studies with mice have various advantages compared to larger rodents such as rats. In general, the shorter life span of mice than rats allows us to investigate progression of diseases or effects of novel treatments within a shorter period of time. In addition, a number of genetic models of disease, including transgenics and knockouts, have been developed in mice; these animals exhibit the specific pathophysiology relevant to the diseases of interest. Other noteworthy advantages of mice over larger-animal models such as rats are that mice are less expensive and easier to manage.

SPECT has coarser sensitivity than PET. However, by using a pinhole collimator with a small pinhole diameter and large magnification factor, SPECT can achieve a full-width half-maximum (FWHM) spatial resolution of less than 1 mm, which is actually superior to that of small-animal PET scanners and well suited for studies of mice [7–12]. SPECT also has the advantage of utilizing radionuclides with longer physical half-lives than those typically used in PET, allowing assessment of longer-term radiotracer distributions and changes therein; longer-lived positron emitters such as copper-64 (^{64}Cu), zirconium-89 (^{89}Zr) and iodine-124 (^{124}I) are adaptable to such applications, but are not yet widely available.

Regional cerebral blood flow (rCBF) can be evaluated using various radiotracers such as radioiodinated iodoantipyrine (IAP) and *N*-isopropyl-4-iodoamphetamine (IMP) and may be a useful descriptor of pathophysiological status and for monitoring of response to various therapeutic interventions, including therapies for cerebral infarctions. ^{123}I-IMP is particularly well suited for measuring blood flow and is often used in clinical SPECT studies due to a relatively high first-pass extraction fraction and a high affinity for brain tissue [13–15].

Several investigators have attempted to measure cerebral blood flow of rodents using pinhole SPECT [16–18]. Seo et al. [16] performed ^{99m}Tc-exametazime SPECT imaging in rat models of ischemic stroke but only evaluated the regional pattern of SPECT image and did not quantitate absolute CBF. Choquet et al. [17] used ^{99m}Tc-(D,L)-hexa-methyl-propylene-amine oxime (^{99m}Tc-HMPAO) and measured a global CBF of 1.10±0.11 ml/g per minute in rats. Pissarek et al. [18] observed the cerebral distribution of ^{99m}Tc-HMPAO in mice using a pinhole SPECT camera, but that study did not measure the absolute CBF. Although a number of studies have measured rCBF in mice using autoradiography [3,4], to our knowledge no studies have measured the absolute rCBF in mice using pinhole SPECT.

In the current study, we performed an ex vivo SPECT study [19], i.e., extracting the mouse's brain and deriving 3D volumetric CBF images using a pinhole SPECT system. Specifically, the feasibility of quantitating the 3D distribution of rCBF in a murine model of cerebral infarction with a high-resolution pinhole SPECT system and ^{123}I-IMP was evaluated.

2. Materials and methods

2.1. Pinhole SPECT system

In pinhole SPECT, magnification yields high-resolution imaging of small objects. As shown in Fig. 1, our pinhole SPECT system consists of a rotating stage, a conventional gamma camera (GCA-7200A, Toshiba, Japan) and a pinhole collimator that is fitted onto the gamma camera [20]. In order to avoid misaligning the center of rotation (COR) due to rotation of the heavily collimated detector assembly, we acquired the projection data by rotating the small mouse brain instead of the camera [20]. The focal length, or the distance from the surface of the camera crystal to the pinhole, is 251 mm. A tungsten pinhole insert with an aperture with a diameter of 1 mm and an opening angle of 60° was used. The non-uniformity of response of the pinhole collimator was corrected using a sensitivity map acquired with a thin flood-source phantom filled with ^{123}I-IMP solution.

In SPECT studies of both phantoms and mice, all projection data were acquired using a 20% energy window centered on 159 keV for ^{123}I, a 15-mm radius of rotation (ROR), a 4.3×4.3-mm pixel size (128×128 matrix), a 360° single circular orbit and 120 projection angles. The magnification factor was 16.7. The SPECT field of view (FOV) was 15 mm in diameter. SPECT images were reconstructed using the pinhole 3D ordered subsets expectation maximization (3D-OSEM) method with eight subsets and two iterations [21]. The reconstructed image set was comprised of an 80×80×80 matrix with voxel size of 0.27×0.27×0.27 mm.

2.2. Phantom experiments

We performed phantom studies in order to evaluate the spatial resolution, uniformity and sensitivity of our system under the acquisition conditions used in our animal experiments.

2.2.1. Line source phantom

The FWHM of the line spread function (LSF) was measured in reconstructed images using a ^{123}I-IMP (37 kBq) line source phantom with a 0.18-mm inner diameter. The phantom was aligned with the axis of rotation and scanned for 8 h with one rotation.

2.2.2. Cylindrical uniform phantom scan

In order to evaluate the sensitivity and uniformity of the SPECT camera, a cylindrical uniform phantom (8.9-mm inner diameter and 8-mm height) filled with ^{123}I-IMP (4.57 MBq in 0.5 ml) was scanned for an hour with one rotation under the same acquisition conditions as the mouse brain scan described below. After the scan, the activity concentration in the phantom was measured using a well counter system (BeWell Model QS-01, Molecular Imaging Labo,

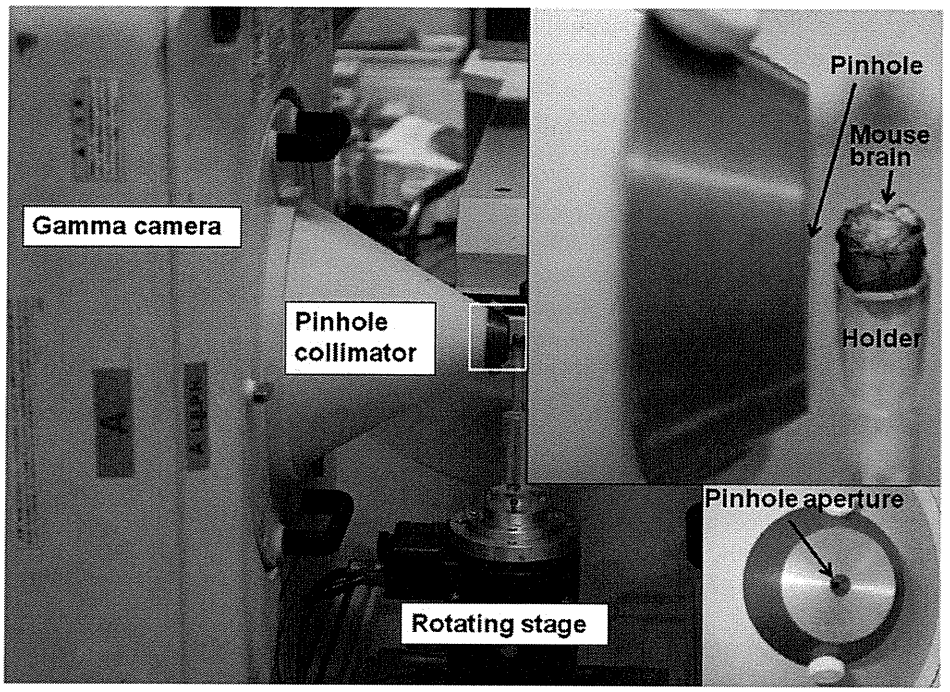

Fig. 1. Photograph of our pinhole SPECT system and a mouse brain sample positioned for imaging. The photograph in the insert (upper right) shows an enlarged view of the pinhole aperture and the brain sample. The photograph in the insert (lower right) shows the pinhole aperture from the front view.

Inc., Japan) in order to obtain a cross-calibration factor (CCF) between the SPECT image count and the activity concentration measured by the well counter. This CCF was later used to quantify the SPECT images of mice.

2.3. Mice studies

2.3.1. Subjects

We studied six male severe combined immunodeficiency mice (8–10 weeks old, 25–35 g) with induced cerebral infarcts. Permanent focal cerebral infarctions in the middle cerebral artery (MCA) cortex were produced by ligating and disconnecting the distal portion of the left MCA [22]. The infarction was created over a period of 9 days before the start of the SPECT experiments. Experiments were carried out following a protocol approved by the Local Committee for Laboratory Animal Welfare, National Cardiovascular Center, Osaka, Japan.

2.3.2. SPECT Scans

Each mouse was anesthetized with halothane. ^{123}I-IMP (16.3–17.4 MBq in 0.1 ml) was administered via the tail vein, and 12–23 min after injection of ^{123}I-IMP the mouse was euthanized, and the brain and skull were extracted. Extracted brains were used in order to maximize the spatial resolution. The brain was placed inside a holder on a rotating stage (Fig. 1). Each brain was scanned for 1 h with one rotation. To calibrate the standard input function described below, 0.3-ml arterial blood was sampled from the left heart chamber when the mouse was euthanized. The activity concentration in the sampled blood was measured using the well counter system, which had been calibrated to the SPECT image using the CCF.

2.3.3. X-ray CT scans

After the SPECT scan, an X-ray CT image of the mouse brain was acquired. This image was used to help align the SPECT and MR images. An angiography system (OEC9800, GE, USA) and a rotating stage [23] were used for this purpose. The maximum tube voltage and tube current were 50 kVp and 0.61 mA, respectively. Data from 300 projections were obtained, and a filtered back-projection algorithm was employed for image reconstruction.

2.3.4. MRI Scans

In order to determine the infarcted area, we used an MR image that was aligned to the SPECT image. The brains of all halothane-anesthetized mice were scanned using an MRI scanner (Signa 3 Tesla, GE, USA) [24] the day before the SPECT study. T2-weighted images were obtained with a two-dimensional fast spin-echo sequence and the following imaging parameters: repetition time: 4000 ms; echo time: 75.4 ms; pixel size: 0.156×0.156×1.0 mm; acquired matrix: 128×90 with 10 slices; transaxial FOV: 20×14 mm; axial FOV: 10 mm; and acquisition time: 13 min 4 s.

2.3.5. Acquisition of arterial input function

In order to compute rCBF, it is generally necessary to obtain the arterial input function by frequent sampling of arterial blood. However, for a small animal such as a mouse, frequent sampling of blood dramatically alters the physiological conditions and significantly perturbs the animals.

Therefore, we used a standardized arterial input function instead of one that had been individually obtained. A standardized arterial input function was obtained from three groups of five mice (ddY mice, total N=15, 4–6 weeks old, 28–32 g) by sequentially sampling the arterial blood following ^{123}I-IMP administration. The first, second and third groups of mice were used to obtain frequent samples for 0–2, 2–8 and 8–60 min, respectively. A 111-MBq dose of ^{123}I-IMP (approximately 0.5 ml) was infused into the tail vein continuously at a constant infusion rate for a period of 1.0 min. In the first group, arterial blood samples were withdrawn every 20 s. In the second group, the samples were withdrawn every 20 s for 2-3 min and additional samples were taken at 5 and 8 min. In the third group, the blood was sampled at 8, 10, 20, 30 and 60 min. From each sample, the lipophilic component was extracted by octanol and its activity concentration was measured using an automated well counter system (AccuFLEXγ7001, ALOKA, Japan).

2.4. Data processing

2.4.1. Computation of rCBF image

A one-tissue compartmental model [13–15] was employed to compute rCBF. With this model, the activity concentration in the brain at time t [i.e. $C_t(t)$ (in MBq/ml)], which can be obtained from SPECT counts multiplied by the CCF, is expressed as:

$$C_t(t) = f \cdot C_a(t) \otimes e^{-\frac{f}{V_d} \cdot t} \quad (1)$$

where $C_a(t)$ is the arterial input function, f is the rCBF (in milliliters of blood per minute per gram of tissue), V_d is the regional distribution volume of ^{123}I-IMP (in ml/ml) and ⊗ is the convolution integral. The value of V_d was assumed to be 45 ml/ml [25]. The voxel-by-voxel rCBF image was calculated from a single SPECT scan by the look-up table technique [14,15,25]. The standardized input function was employed as $C_a(t)$ in Eq. (1). The whole-blood activity concentration of a single-blood sample was used to calibrate this standard input function.

2.4.2. Alignment of SPECT and MR images using X-ray CT images

The X-ray CT image was used to align SPECT images with MR images. As the skull was clearly depicted on the X-ray CT image, it facilitates alignment of the SPECT and MRI images. The original MR image had muscle and skin components; an image of the brain alone was extracted from the original image, using software implemented on FSL version 4.1 (*F*MRIB *S*oftware *L*ibrary, FMRIB Center, Oxford University). Fig. 2 shows the procedure used for the alignment of SPECT and MR images. First, all the images were adjusted to have a pixel size of 0.1 mm. Second, the brain SPECT and MR images were aligned with the skull on the X-ray CT images. Alignment was performed by shifting and rotating the images using the AMIDE image display and analysis software [26] and visual inspection. Following alignment, the region of interest (ROI) drawn on the MR image set was superimposed on the SPECT and the CBF image sets.

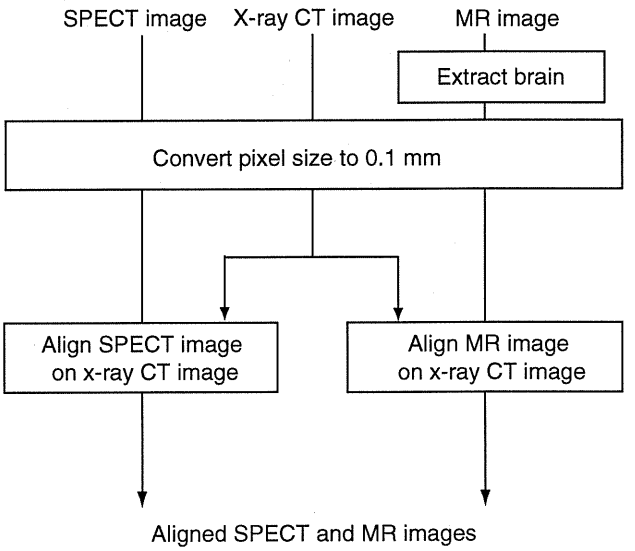

Fig. 2. Procedure for alignment of SPECT and MR images (see text for further details).

2.4.3. Data analysis

The infarcted area was defined as the high-intensity area on the post-stroke T2-weighted MRI image, as determined by visual inspection, and was outlined manually. The mean CBF value within the ROI of this infarcted region was obtained from aligned SPECT-CBF images. As a control, we obtained the mean CBF values from the ROI in the contralateral non-infarcted region. This contralateral ROI was made by flipping the infarcted ROI in the right–left direction (see Fig. 3). The CBF values of the infarcted and control regions were evaluated in all six mice. Data dispersion was expressed as the standard deviation (SD).

3. Results

3.1. Experiments with phantoms

According to the measurement of spatial resolution of our system, the LSF of the ^{123}I-IMP line source on the reconstructed image had a FWHM of 0.91 mm.

Fig. 4 shows the transverse, coronal and sagittal SPECT images of the cylindrical uniform phantom and their corresponding count profiles across the images. As shown in this figure, we obtained SPECT images with a uniform distribution within the FOV. The uniform activity distribution was also reflected by the flat count profiles. The sensitivity was 167.1 cps/MBq.

3.2. Experiments with mice

Fig. 5 shows the standard input function obtained by averaging the whole-blood activity concentrations of five samples taken at different time points. Fig. 3A and B shows the MR and SPECT images with infarct, respectively,

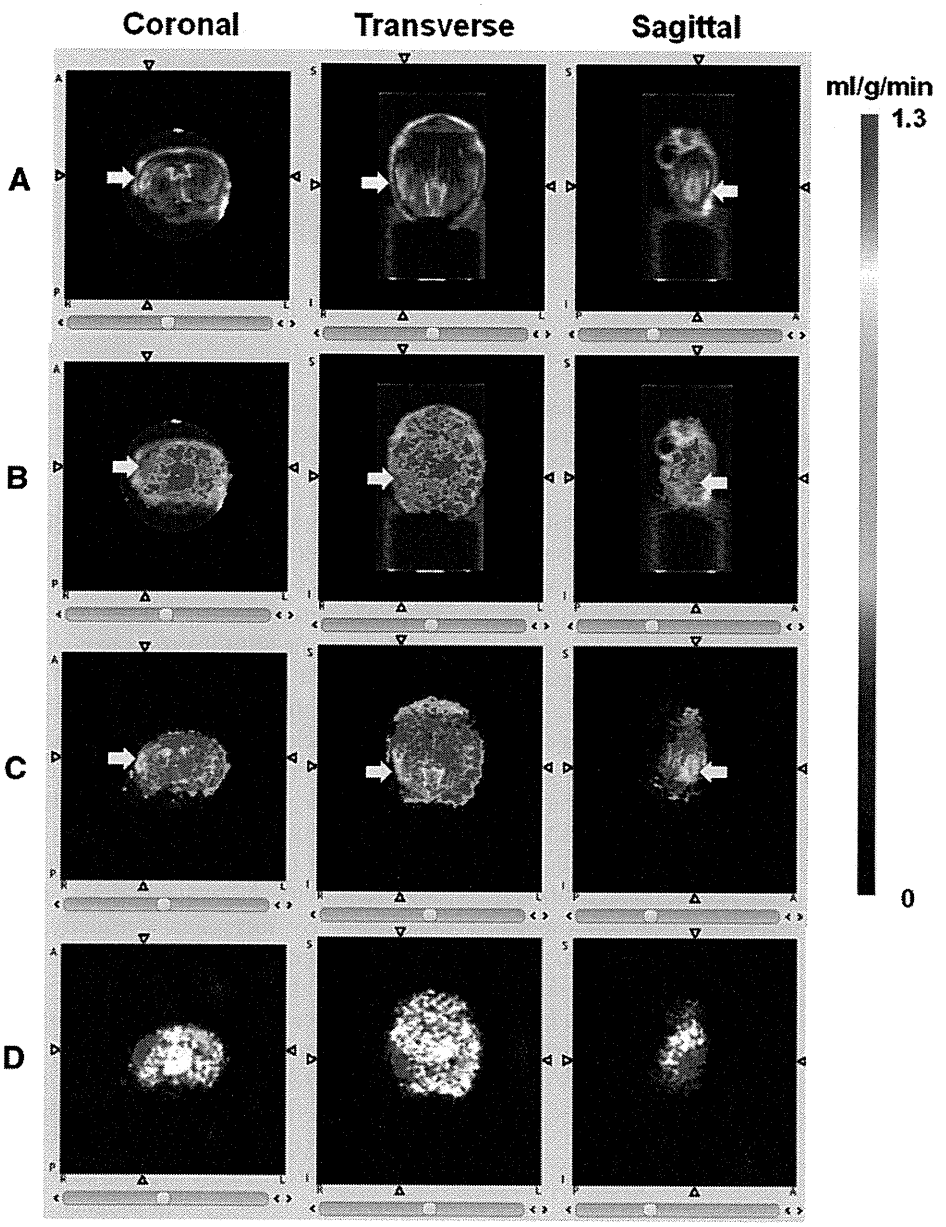

Fig. 3. Representative aligned images and ROIs drawn on CBF images. A gray scale, a hot-metal color scale and a rainbow color scale are used to display X-ray CT, MR and CBF images, respectively. The MR image was digitally processed to remove skin and muscle. (A) MR image superimposed on the X-ray CT image. (B) CBF image superimposed on the X-ray CT image. (C) Superimposition of MR and CBF images. Arrows indicate infarcted areas. The attached color scale bar is for CBF images in (B) and (C). (D) CBF image and ROIs (red: infarcted area; green: region opposite the infarcted area). These ROIs were determined from the MR image.

superimposed on the CT image. As shown in Fig. 3C, the CBF images computed from SPECT images appear accurately aligned with the MRI images using our image alignment scheme. The CBF images showed defects in the infarcted area depicted by the MR images. Fig. 3D shows ROIs drawn on the CBF image. These ROIs were determined from the MR images. The volume of the infarcted area in the MR image set was 18.4±6.0 mm^3.

The CBF values in infarcted regions were 0.61±0.20 ml/g per minute, as compared to 0.91±0.27 ml/g per minute in control regions. The foregoing difference in CBF between the infarcted and the control regions was statistically significant (Student's t test: $P<0.05$). Thus, our system demonstrated that the CBF decreases in the infarcted region.

4. Discussion

Phantom studies demonstrated that 3D high-resolution SPECT imaging could be achieved with 0.9-mm FWHM

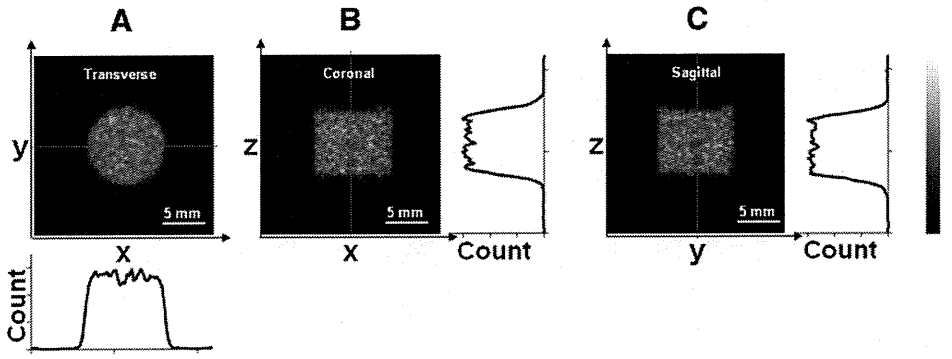

Fig. 4. Transverse, coronal and sagittal SPECT images of the cylindrical uniform phantom and their corresponding count profiles across the images. Each profile is along the line on the image. (A) Transverse image; profile was generated from an average of 25 slices in the *Z* direction. (B) Coronal image; profile was generated from an average of 30 slices in the *Y* direction. (C) Sagittal image; profile was generated from an average of 30 slices in the *X* direction.

spatial resolution and uniform sensitivity throughout the volume imaged. Thus, our system is applicable to quantitative assessment of physiological parameters in the mouse brain. Our pinhole SPECT system utilized a conventional clinical SPECT camera with ^{123}I-IMP and provided absolute rCBF measurements in extracted brain derived from a mouse cerebral infarct model.

Despite its coarser resolution, our methodology has some advantages over autoradiography. Unlike autoradiography, this approach yields a 3D parametric map that can be superimposed on images from other modalities such as MRI. The use of such anatomic images registered with the functional SPECT image set often allows more objective and reliable delineation of pertinent ROIs. Other applications of our system include voxel-based statistical analysis, such as statistical parametric mapping, which may also allow objective evaluation of regional changes without a priori ROIs. Another advantage of our system is shortening of the overall study time. The study with our system is completed within half a day, while autoradiography with ^{125}I takes several days for exposure. In addition, for centers without a dedicated small-animal SPECT system, application of a clinical pinhole SPECT system to high-resolution imaging of the harvested mouse brain (or other specimen) utilizing a rotating specimen stage can eliminate COR misalignment and image degradation associated with rotation of the heavy detector assembly [20]. However, our methodology is not specific to single-pinhole SPECT systems but can be applied to modern small-animal SPECT.

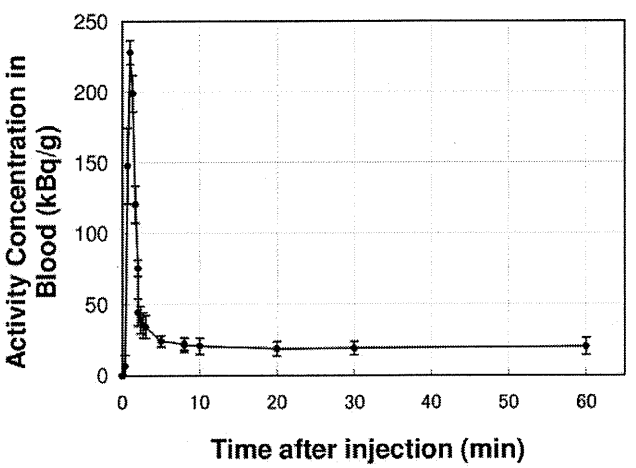

Fig. 5. Population-based standardized arterial input function obtained from five mice by sequentially sampling the arterial blood following IMP administration. Circle plots indicate the mean of whole-blood activity concentrations from five samples at each point. The counting efficiency of the well counter system is 0.73. Error bars indicate the standard errors of the means.

There are some limitations with our current system. The low sensitivity of single-pinhole imaging is one such limitation. By increasing sensitivity, noise in the image will be suppressed and one can expect to more easily distinguish differences in CBF between the infarcted and the control regions. The technique presented is not limited solely to single-aperture pinhole imaging but is adaptable to multi-pinhole (coded aperture) systems, although the latter are associated with so-called multiplexing artifacts associated with overlap of the projection images [27].

In the current study, the geometric distortion associated with pinhole imaging was minimal because of the small volume being imaged, that of the mouse brain. Such distortion may be more pronounced, however, if adapting this method to measurement of blood flow in larger volumes such as certain organs or tumors. This distortion may nonetheless be avoided or at least minimized by helical-orbit [28] or two-circular orbit scanning [20,21].

It is important to assess regional CBF changes in evaluating therapeutic response to various treatments. For regional determination of the infarcted area, it is essential to align the SPECT and MR images. For small-animal imaging, there are several commercially available hybrid SPECT scanners with X-ray CT cameras. However, it is difficult to determine the infarcted area using the X-ray CT image. The registration technique presented in this article is applicable to many image modalities, including MR. The direct registration of the SPECT and MR image sets is not feasible because of the coarser resolution and generally lower contrast of the

former relative to the latter. The registration was achieved, however, via the CT image set. As in the 'head-and-hat' registration technique [29], the brain visualized on the SPECT and MR images can be fitted just inside the skull as visualized on the CT images.

It is sometimes useful to evaluate absolute rCBF rather than the pattern of distribution of a blood-flow radiotracer, as in the case of multi-group comparisons. To obtain absolute CBF measurements, PET studies with ^{15}O-water are often performed [30]. However, the positron emitted by ^{15}O has a relatively long range, which degrades PET spatial resolution and therefore may make ^{15}O-water unsuitable for CBF studies in mice. Moreover, ^{123}I-IMP is widely available commercially, and more widely available than ^{15}O-water, in Japan and elsewhere. Clinical pinhole SPECT systems are likewise more widely available than small-animal PET scanners. Finally, mice are less expensive and easier to house and manage than rats.

Maeda et al. [4] measured rCBF values of mice using ^{14}C-iodoantipyrine and autoradiography. They reported rCBF values of mice that ranged between 0.50 and 1.63 ml/g per minute; their results were consistent with ours for the control region (0.91 ml/g per minute). Moreover, the inter-subject variability of our results was ~30%, which is also consistent with their data. In the future, it will be necessary to directly compare rCBF measured by our approach and by the autoradiographic approach.

In this study, we used the standard input function instead of the individual input function. For quantitative rCBF measurements, it is preferable to use an individual input function by frequent sampling of arterial blood. However, for small animals such as mice, CBF could be changed by frequent blood sampling during SPECT acquisition. Utilization of a standard input function is widely accepted in clinical studies that use ^{123}I-IMP to compute rCBF [14]. The standard input function was generated from the activity concentration in the lipophilic component extracted by octanol; however, the octanol extraction was not performed on blood samples taken during the SPECT scan. Moreover, due to manual administration of ^{123}I-IMP during SPECT studies, there was no guarantee that the shapes of the individual input function and the standard input function were the same. In addition, the V_d value of 45 ml/ml was determined from human studies [25] and it may be different for mice. Therefore, the CBF values calculated in this study may be biased. Furthermore, the lipophilic component might vary among subjects and lead to inter-subject variability in the CBF value.

We designed the pinhole SPECT system with a high resolution (less than 1 mm) for mouse imaging. The CBF value in the infarcted region was lower than the CBF value in the control region, but the absolute CBF value in the infarcted region still seemed to be overestimated. This is probably due to the partial volume effect; alternatively, the spatial resolution might not have been sufficient for reliable measurements in a source volume as small as a mouse brain. One potential source of degraded spatial resolution might have been high-energy photons (>500 keV) emitted by ^{123}I, which penetrated the pinhole collimator [31].

Our study was an ex vivo SPECT study rather than an in vivo SPECT study. It is possible to scan the head of a living mouse by improving our SPECT system. However, the spatial resolution and count statistics will be degraded because the head of a living mouse is larger than an extracted brain; therefore, a longer ROR would be required, resulting in lower sensitivity and coarser spatial resolution. For instance, if the ROR is increased from 15 to 30 mm in order to double the area of the FOV and visualize an entire mouse head, the sensitivity will be reduced by 75% and the spatial resolution doubled. A combination of a pinhole with large aperture and software-based resolution recovery techniques would be one solution for improving sensitivity as well as spatial resolution. The use of a 2-mm pinhole instead of a 1-mm pinhole will increase the sensitivity fourfold in proportion to the area of the pinhole aperture. Several resolution recovery techniques have been proposed, including the collimator blurring model-based resolution recovery method [32,33] and the MRI-based resolution recovery method [34–36]. In the future, we expect that acquisition of the CBF map from a living mouse brain using our pinhole SPECT system could be achieved by means of a software-based resolution recovery method. In vivo small-animal SPECT can measure the same animal quantitatively, non-invasively and repeatedly [5]. Therefore, it allows us to reduce the number of small laboratory animals required in typical longitudinal studies, drug development or the assessment of new therapies. As shown in this study, there was large variability (32.5%) in the infarcted volume, and in vivo studies can eliminate the inter-subject variability by individually monitoring CBF changes in successive studies. In addition, this approach could provide a link between the animal model and human studies.

5. Conclusion

This study demonstrated the feasibility of the 3D quantitation of rCBF in mice using high-resolution pinhole SPECT and ^{123}I-IMP. The 3D parametric map allows superimposition of images from other modalities as well as objective analysis. In the future, we expect that our SPECT system will be able to perform quantitative measurement of rCBF in living mice.

References

[1] Miekle SR, Eberl S, Iida H. Instrumentation and methodology for quantitative pre-clinical imaging studies. Curr Pharm Des 2001;7: 1945–66.

[2] Sakurada O, Kennedy C, Jehle J, Brown JD, Carbin GL, Sokoloff L. Measurement of local cerebral blood flow with iodo[^{14}C]antipyrine. Am J Physiol 1978;234:H59–66.

[3] Jay TM, Lucignani G, Crane AM, Jehle J, Sokoloff L. Measurement of local cerebral blood flow with [^{14}C]iodoantipyrine in the mouse. J Cereb Blood Flow Metab 1988;8:121–9.
[4] Maeda K, Mies G, Oláh L, Hossmann KA. Quantitative measurement of local cerebral blood flow in the anesthetized mouse using intraperitoneal [^{14}C]iodoantipyrine injection and final arterial heart blood sampling. J Cereb Blood Flow Metab 2000;20:10–4.
[5] Chatziioannou AF. PET scanners dedicated to molecular imaging of small animal models. Mol Imaging Biol 2002;4:47–63.
[6] Peremans K, Cornelissen B, Van Den Bossche B, Audenaert K, Van de Wiele C. A review of small animal imaging planar and pinhole SPECT γ camera imaging. Vet Radiol Ultrasound 2005;46:162–70.
[7] Miekle SR, Kench P, Kassiou M, Banati RB. Small animal SPECT and its place in the matrix of molecular imaging technologies. Phys Med Biol 2005;50:R45–61.
[8] Acton PD, Choi SR, Plössl K, Kung HF. Quantification of dopamine transporters in the mouse brain using ultra-high resolution single-photon emission tomography. Eur J Nucl Med 2002;29:691–8.
[9] Acton PD, Hou C, Kung MP, Plössl K, Keeney CL, Kung HF. Occupancy of dopamine D_2 receptors in the mouse brain measured using ultra-high-resolution single-photon emission tomography and [^{123}I]IBF. Eur J Nucl Med 2002;29:1507–15.
[10] Wu MC, Tang HR, Gao DW, Ido A, O'Connell JW, Hasegawa BH, et al. ECG-gated pinhole SPECT in mice millimeter spatial resolution. IEEE Trans Nucl Sci 2000;47:1218–21.
[11] Constantinesco A, Choquet P, Monassier L, Israel-Jost V, Mertz L. Assessment of left ventricular perfusion, volumes, and motion in mice using pinhole gated SPECT. J Nucl Med 2005;46:1005–11.
[12] Beekman FJ, van der Have F, Vastenhouw B, van der Linden AJ, van Rijk PP, Burbach JP, et al. U-SPECT-I: a novel system for submillimeter-resolution tomography with radiolabeled molecules in mice. J Nucl Med 2005;46:1194–200.
[13] Kuhl DE, Barrio JR, Huang SC, Selin C, Ackermann RF, Lear JL, et al. Quantifying local cerebral blood flow by *N*-isopropyl-*p*-[^{123}I]iodoamphetamine (IMP) tomography. J Nucl Med 1982;23:196–203.
[14] Iida H, Itoh H, Nakazawa M, Hatazawa J, Nishimura H, Onishi Y, et al. Quantitative mapping of regional cerebral blood flow using iodine-123-IMP and SPECT. J Nucl Med 1994;35:2019–30.
[15] Iida H, Itoh H, Bloomfield PM, Munaka M, Higano S, Murakami M, et al. A method to quantitate cerebral blood flow using a rotating gamma camera and iodine-123 iodoamphetamine with one blood sampling. Eur J Nucl Med 1994;21:1072–84.
[16] Seo Y, Gao DW, Hasegawa BH, Dae MW, Franc BL. Rodent brain imaging with SPECT/CT. Med Phys 2007;34:1217–20.
[17] Choquet P, Israel-Jost V, Namer J, Bilbault P, Schneider F, Constantinesco A. CBF imaging and global CBF quantification in normal rats using dedicated pinhole SPECT system. J Cereb Blood Flow Metab 2005;25:S527 (Abstract).
[18] Pissarek MB, Oros-Peusquens AM, Schramm NU. Challenge by the murine brain: multi-pinhole SPECT of ^{123}I-labelled pharmaceuticals. J Neurosci Methods 2008;168:282–92.
[19] Terrovitis J, Kwok KF, Lautamäki R, Engles JM, Barth AS, Kizana E, et al. Ectopic expression of the sodium-iodide symporter enables imaging of transplanted cardiac stem cell in vivo by single-photon emission computed tomography or positron emission tomography. J Am Coll Cardiol 2008;52:1652–60.
[20] Aoi T, Zeniya T, Watabe H, Deloar HM, Matsuda T, Iida H. System design and development of a pinhole SPECT system for quantitative functional imaging of small animals. Ann Nucl Med 2006;20:245–51.
[21] Zeniya T, Watabe H, Aoi T, Kim KM, Teramoto N, Hayashi T, et al. A new reconstruction strategy for image improvement in pinhole SPECT. Eur J Nucl Med Mol Imaging 2004;31:1166–72.
[22] Taguchi A, Soma T, Tanaka H, Kanda T, Nishimura H, Yoshikawa H, et al. Administration of CD34+ cells after stroke enhances neurogenesis via angiogenesis in a mouse model. J Clin Invest 2004;114:330–8.
[23] Onodera H, Watabe H, Minato K, Iida H. Flow analysis system for leukocyte removal column. Med Imag Tech 2007;25:277–83.
[24] Yamamoto A, Sato H, Enmi J, Ishida K, Ose T, Kimura A, et al. Use of a clinical MRI scanner for preclinical research on rats. Radiol Phys Technol 2009;2:13–21.
[25] Iida H, Akutsu T, Endo K, Fukuda H, Inoue T, Ito H, et al. A multicenter validation of regional cerebral blood flow quantitation using [^{123}I]iodoamphetamine and single photon emission computed tomography. J Cereb Blood Flow Metab 1996;16:781–93.
[26] Loening AM, Gambhir SS. AMIDE: A free software tool for multimodality medical image analysis. Mol Imag 2003;2:131–7.
[27] Nuyts J, Vunckx K, Defrise M, Vanhove C. Small animal imaging with multi-pinhole SPECT. Methods 2009;48:83–91.
[28] Metzler SD, Greer KL, Jaszczak RJ. Helical pinhole SPECT for small-animal imaging: a method for addressing sampling completeness. IEEE Trans Nucl Sci 2003;50:1575–783.
[29] Pelizzari CA, Chen GT, Spelberg DR, Weichselbaum RR, Chen CT. Accurate three-dimensional registration of CT, PET, and/or MR images of the brain. J Comput Assist Tomogr 1989;13:20–6.
[30] Yee SH, Jerabek PA, Fox PT. Non-invasive quantification of cerebral blood flow for rats by microPET imaging of ^{15}O labeled water: the application of a cardiac time-activity curve for the tracer arterial input function. Mucl Med Comm 2005;26:903–11.
[31] Deloar HM, Watabe H, Aoi T, Iida H. Evaluation of penetration and scattering components in conventional pinhole SPECT: phantom studies using Monte Carlo simulation. Phys Med Biol 2003;48:995–1008.
[32] Beque D, Vanhove C, Andreyev A, Nuyts J, Defrise M. Correction for imperfect camera motion and resolution recovery in pinhole SPECT. 2004 IEEE Nuclear Science Symposium Conference Record, Vol. 4; 2004, pp. 2507–10.
[33] Vanhove C, Andreyev A, Defrise M, Nuyts J, Bossuyt A. Resolution recovery in pinhole SPECT based on multi-ray projections: a phantom study. Eur J Nucl Med Mol Imaging 2007;34:170–80.
[34] Mameuda Y, Kudo H. New anatomical-prior-based image reconstruction method for PET/SPECT. 2007 IEEE Nuclear Science Symposium Conference Record, Vol. 6; 2007, pp. 4142–8.
[35] Quarantelli M, Berkouk K, Prinster A, Landeau B, Svarer C, Balkay L, et al. Integrated software for the analysis of brain PET/SPECT studies with partial-volume-effect correction. J Nucl Med 2004;45: 192–201.
[36] Wells RG. Anatomical priors to improve image quality in small-animal SPECT/CT. 2007 IEEE Nuclear Science Symposium Conference Record, Vol. 6; 2007, pp. 4319–23.

SYNAPSE 65:751–762 (2011)

Sensitivity of Kinetic Macro Parameters to Changes in Dopamine Synthesis, Storage, and Metabolism: A Simulation Study for [^{18}F]FDOPA PET By a Model With Detailed Dopamine Pathway

KEISUKE MATSUBARA,[1,2,3] HIROSHI WATABE,[4]* YOSHITAKA KUMAKURA,[5] TAKUYA HAYASHI,[6] CHRISTOPHER J. ENDRES,[7] KOTARO MINATO,[1] AND HIDEHIRO IIDA[2]

[1]*Department of Bioinformatics and Genomics, Graduate School of Information Science, Nara Institute of Science and Technology, Takayama, Ikoma, Nara 630-0192, Japan*

[2]*Department of Investigative Radiology, Advanced-Medical Engineering Center, National Cardiovascular Center, Fujishiro-dai, Suita, Osaka 565-8565, Japan*

[3]*Department of Radiology and Nuclear Medicine, Research Institute of Brain and Blood Vessels Akita, Senshu-Kubota-machi, Akita, Akita 010-0874, Japan*

[4]*Department of Molecular Imaging in Medicine, Graduate school of Medicine, Osaka University, Yamadagaoka, Suita, Osaka 565-0871, Japan*

[5]*Research Center for Advanced Science and Technology, The University of Tokyo, Tokyo, Japan*

[6]*Functional Probe Research Laboratory, RIKEN Center for Molecular Imaging Science, Kobe, Hyogo, Japan*

[7]*The Russell H. Morgan Department of Radiology and Radiological Science, Johns Hopkins University School of Medicine, Baltimore, Maryland 21287*

KEY WORDS positron emission tomography; [^{18}F]FDOPA; kinetic analysis; dopamine

ABSTRACT Quantitative interpretation of brain [^{18}F]FDOPA PET data has been made possible by several kinetic modeling approaches, which are based on different assumptions about complex [^{18}F]FDOPA metabolic pathways in brain tissue. Simple kinetic macro parameters are often utilized to quantitatively evaluate metabolic and physiological processes of interest, which may include DDC activity, vesicular storage, and catabolism from ^{18}F-labeled dopamine to DOPAC and HVA. A macro parameter most sensitive to the changes of these processes would be potentially beneficial to identify impaired processes in a neurodegenerative disorder such as Parkinson's disease. The purpose of this study is a systematic comparison of several [^{18}F]FDOPA macro parameters in terms of sensitivities to process-specific changes in simulated time-activity curve (TAC) data of [^{18}F]FDOPA PET. We introduced a multiple-compartment kinetic model to simulate PET TACs with physiological changes in the dopamine pathway. TACs in the alteration of dopamine synthesis, storage, and metabolism were simulated with a plasma input function obtained by a non-human primate [^{18}F]FDOPA PET study. Kinetic macro parameters were calculated using three conventional linear approaches (Gjedde-Patlak, Logan, and Kumakura methods). For simulated changes in dopamine storage and metabolism, the slow clearance rate (k_{loss}) as calculated by the Kumakura method showed the highest sensitivity to these changes. Although k_{loss} performed well at typical ROI noise levels, there was large bias at high noise level. In contrast, for simulated changes in DDC activity it was found that K_i and V_T, estimated by Gjedde-Patlak and Logan method respectively, have better performance than k_{loss}. **Synapse 65:751–762, 2011.** ©2010 Wiley-Liss, Inc.

INTRODUCTION

[^{18}F]6-fluoro-L-3, 4-dihydroxyphenylalanine ([^{18}F]FDOPA) is a ^{18}F-labeled analog of L-dopa, the endogenous precursor of dopamine. Positron emission tomography (PET) scan with [^{18}F]FDOPA is applied for monkey and human to investigate the integrity of dopaminergic neurons in Parkinson's disease (Brooks,

Contract grant sponsor: Grant for Research on Psychiatric and Neurological Diseases and Mental Health [Ministry of Health, Labor, and Welfare (MHLW), Japan]; Contract grant number: H17-025; Contract grant sponsor: The Program for Promotion of Fundamental Studies in Health Sciences of the National Institute of Biomedical Innovation (NIBIO), Japan; Contract grant number: 05-6. Contract grant sponsor: Strategic International Cooperative Program (Research Exchange Type), Japan Science and Technology Agency (JST), Japan.

*Correspondence to: Hiroshi Watabe, Department of Molecular Imaging in Medicine Osaka University Graduate School of Medicine, 2-2 Yamadaoka, Suita, Osaka 565-0871 Japan. E-mail: watabe@mi.med.osaka-u.ac.jp

Received 11 October 2010; Accepted 2 December 2010

DOI 10.1002/syn.20899

Published online 28 December 2010 in Wiley Online Library (wileyonlinelibrary.com).

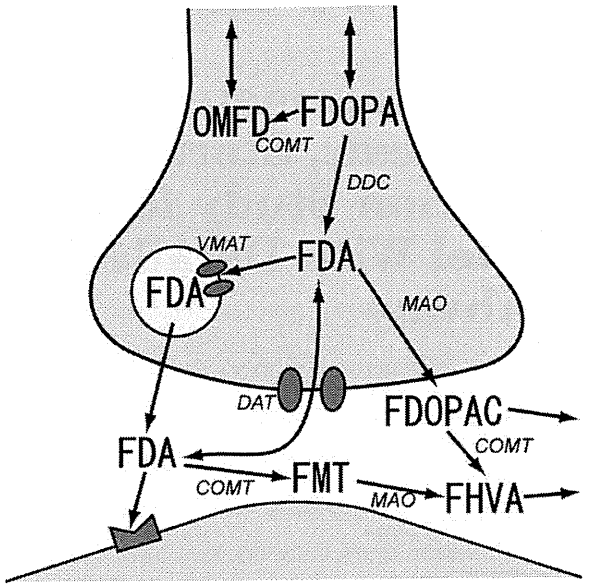

Fig. 1. Metabolic pathway in dopamine nerve.

2004; Cheesman et al., 2005; Cumming and Gjedde, 1998; de la Fuente-Fernandez et al., 2000; Hilker et al., 2005; Ishikawa et al., 1996; Ito et al., 2002; Kumakura et al., 2005; Morrish et al., 1995; Piccini et al., 2005), as well as other neurological disorders, such as schizophrenia (Kumakura et al., 2007; McGowan et al., 2004; Reith et al., 1994), and epilepsy (Bouilleret et al., 2005).

[^{18}F]FDOPA is decarboxylated to [^{18}F]fluorodopamine ([^{18}F]FDA) by dopa decarboxylase (DDC) in dopaminergic neurons. [^{18}F]FDA may then be transported into synaptic vesicles via vesicle monoamine transporter (VMAT). Stored [^{18}F]FDA is delivered to the synaptic cleft by exocytosis and [^{18}F]FDA in synaptic cleft is re-uptaken to presynaptic cell by dopamine transporter (DAT). Cytosolic [^{18}F]FDA is metabolized to [^{18}F]6-fluoro-3,4-dihydroxyphenyl acetic acid ([^{18}F]FDOPAC), [^{18}F]6-fluoro-3-methoxytyramine ([^{18}F]FMT) and [^{18}F]6-fluoro-homovanilic acid ([^{18}F]FHVA) by monoamine oxidase (MAO) and catechol-*O*-methyltransferase (COMT) (Cooper et al., 2003; Cumming et al., 1987; Firnau et al., 1987). The acidic metabolites, [^{18}F] FDOPAC and [^{18}F]FHVA, are cleared from brain tissue primarily by diffusion into the cerebrospinal fluid (CSF) (Cumming et al., 1987; Firnau et al., 1987) (Fig. 1). Thus, the time course of radioactivity uptake following [^{18}F]FDOPA injection reflects a complex pathway that includes [^{18}F]FDA synthesis, storage, and metabolism. Consequently, kinetic parameters derived from FDOPA PET studies will be sensitive to these processes to varying degrees.

Compartmental analysis with non-linear least square algorithms has been applied to estimate a rate of dopamine synthesis for the kinetic analysis of [^{18}F]FDOPA (Huang et al., 1991; Kuwabara et al., 1993). For a more general representation of FDOPA uptake, several macro parameters have been also used (see Table 1). The net influx of [^{18}F]FDOPA (K_i) has been estimated easily via Gjedde-Patlak graphical analysis in monkey and human [^{18}F]FDOPA PET studies (Bouilleret et al., 2005; Cheesman et al., 2005; Cumming and Gjedde, 1998; de la Fuente-Fernandez et al., 2000; Gjedde, 1981, 1982; Hilker et al., 2005; Ishikawa et al., 1996; Ito et al., 2002; Kumakura et al., 2004; Martin et al., 1989; McGowan et al., 2004; Morrish et al., 1995; Patlak and Blasberg, 1985; Patlak et al., 1983; Piccini et al., 2005; Takagi et al., 2005). Gjedde-Patlak analysis assumes that tracer accumulates irreversibly and the loss of tracer and its metabolites are negligible during the PET scanning period. The physiological mechanism for irreversible accumulation is considered to be the storage of [^{18}F]FDA in synaptic vesicles, where [^{18}F]FDA is protected from metabolic enzymes. However, cytosolic [^{18}F]FDA can be rapidly catabolized by MAO and COMT, and the labeled metabolites diffuse from the brain to CSF rapidly (Cumming et al., 1994). Thus, the assumption of irreversible uptake on Gjedde-Patlak method is not strictly consistent with the physiological profile of [^{18}F]FDOPA.

Extended Gjedde-Patlak graphical analysis, which considers the loss of [^{18}F]FDA metabolites from brain tissue, yields estimates of both the net uptake (K_i) and the clearance of [^{18}F]FDA metabolites from brain tissue (k_{loss}) (Holden et al., 1997; Sossi et al., 2001). A macro parameter termed the effective distribution volume (EDV), defined as the ratio of K_i and k_{loss} (K_i/k_{loss}), was proposed (Sossi et al., 2001) and used as an index for dopamine turnover (Sossi et al., 2002, 2003, 2004, 2007). Recently, Kumakura el al. estimated EDV, k_{loss}, and total distribution volume, which is symbolized as V_T in this article, and V_d in Kumakura et al., 2007, 2010a,b, by a multilinear regression analysis based on the equation derived from rearrangement of "inlet and outlet model" (Kumakura method) (Kumakura et al., 2006, 2007). For studies of sufficient scan duration, Logan graphical analysis (Logan et al., 1990) may be applied (Kawatsu et al., 2002; Kumakura et al., 2005) to estimate V_T in [^{18}F]FDOPA PET.

TABLE I. Definitions of kinetic term for analysis

Terms	Units	Definition
K_i	g/ml/min	Net influx constant for FDOPA. Estimated by Gjedde-Patlak method.
V_T	g/ml	Total distribution volume of FDOPA and its metabolites. Estimated by Logan or Kumakura method.
k_{loss}	min^{-1}	Rate constant for the diffusion of the acidic metabolites of FDA from the tissue. Estimated by Kumakura method.
V_f	g/ml	Distribution volume of precursor pool.
V_b	g/ml	Effective blood volume.

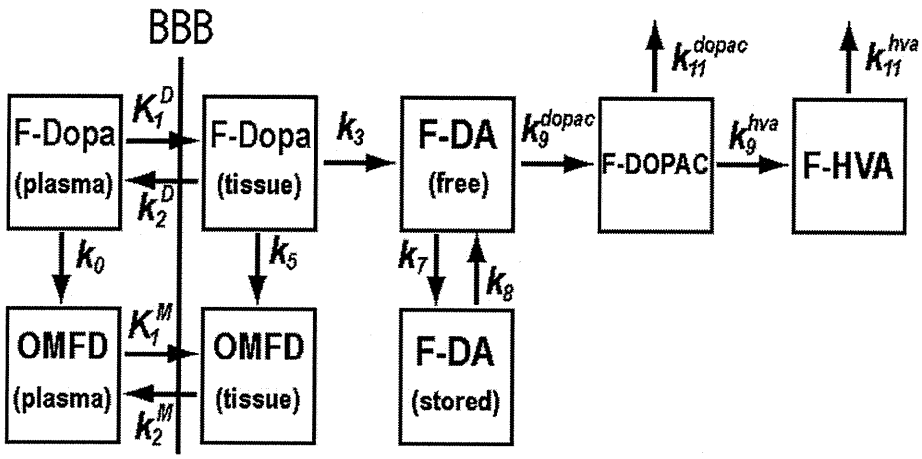

Fig. 2. DF model.

Pathophysiological studies of animal and postmortem brain reported that several changes of dopamine pathway in the striatum were observed in neurodegenerative disorders, for example, Parkinson's disease. The reduction of DDC activity in the striatum of patients with Parkinson's disease has been reported in postmortem (Lloyd and Hornykiewicz, 1970) and PET studies (Gjedde et al., 1993; Ishikawa et al., 1996; Wahl and Nahmias, 1996). Both postmortem and PET studies with a radiolabeled marker for the vesicular monoamine transporter 2 (VMAT2) suggest that the reduction of the capacity for dopamine storage in the vesicle is a key event in the early phase of Parkinson's disease (Borght et al., 1995; Chen et al., 2008; Frey et al., 1996; Lee et al., 2000; Sossi et al., 2007). A further observation is that the ratio between HVA and DA increases in the caudate and putamen of asymptomatic and symptomatic MPTP-induced monkeys, suggesting that dopamine turnover in Parkinson's disease is upregulated (Hornykiewicz and Kish, 1987; Pifl and Hornykiewicz, 2006). The reduction of the capacity for dopamine storage (Frey et al., 1996; Kumakura et al., 2010b) and acceleration of dopamine turnover (Fowler et al., 2002) have been also observed in normal aging.

According to above finding, estimated [18F]FDOPA macro parameter to detect the metabolic changes in dopamine pathways can be a good index for the pathophysiological investigations related to dopamine metabolism and the diagnosis of neurodegenerative disorders. The investigations for capability of macro parameters to detect the changes in dopamine pathway can show us the best model for kinetic parameter estimation in [18F]FDOPA PET study. Pharmacological treatment or computer simulation for dopamine pathway is required to investigate the sensitivity of macro parameters to such a metabolic change. However, the former often affects non-interested processes as well as an interested process in dopamine pathway, and it causes the bias in results. Thus, we selected the simulation method to investigate the sensitivity of macro parameter to the pathophysiological changes in dopamine pathway.

We aimed at comparing the sensitivity of estimated [18F]FDOPA macro parameters to process-specific changes in dopamine pathway by simulation study. For simulation of individual changes in the [18F]FDOPA pathways, we introduced a compartment model: "Detailed FDOPA kinetic model (DF model)" (Fig. 2). The macro parameters, K_i, V_T, and k_{loss}, were obtained from the simulated TACs using three conventional linear regression methods: Gjedde-Patlak graphical analysis, Logan graphical analysis, and Kumakura method. We compared the trends for estimated macro parameters to the changes in DDC activity, dopamine storage, and metabolism as "sensitivity."

MATERIALS AND METHODS

In this study, we evaluated the sensitivity of estimated [18F]FDOPA macro parameters to the changes in dopamine synthesis, storage, and metabolism by the following steps.

1. A control [18F]FDOPA PET study was performed on a monkey, and a TAC in the striatum was obtained.
2. Based on the TAC obtained by monkey PET study, a standard TAC was generated by DF model. The rate constants given in this simulation are similar to values estimated by compartment model analysis of monkey data and values reported previously (Cumming and Gjedde, 1998; Cumming et al., 1994; Deep et al., 1997).
3. For simulation of the changes in the DDC activity, dopamine storage or dopamine metabolism to DOPAC, TACs were calculated with the alteration of k_3, k_7, or k_9^{dopac} to the value given in simulation of standard TAC. Noise observed in actual PET data was added to TACs for realistic evaluation.

4. K_i, V_T, and k_{loss} were estimated from simulated TACs by Gjedde-Patlak, Logan, and Kumakura method.
5. We estimated the sensitivity of macro parameters to changes in dopamine synthesis, storage, and metabolism.

Detailed FDOPA kinetic model (DF model)

The compartment model used in TAC simulations of our study, DF model, is based on the biochemical pathways of dopamine as shown in Figure 1 (Cooper et al., 2003; Cumming et al., 1987; Firnau et al., 1987). DF model (Matsubara et al., 2010) describes dopamine synthesis [compartment "FDA(free)" and rate constant k_3], storage [compartment "FDA(-stored)" and rate constant k_7] and dopamine metabolism to its diffusible metabolites, [^{18}F]FDOPAC and [^{18}F]FHVA (compartment "FDOPAC," "FHVA," and rate constant, k_9^{dopac}, k_9^{hva}) (see Fig. 2). A set of differential equations to describe the exchange processes between compartments are derived such as general compartment model.

Acquisition of standard data as normal condition

An [^{18}F]FDOPA PET scan in a normal monkey was performed to obtain a control striatal TAC and metabolite-corrected arterial input function.

Animal procedures

A normal cynomolgus monkey (macaca fascicularis, body weight: 3.8 kg) was anesthetized by ketamine (8.4 mg, intramuscularly) and xylazine (1.7 mg, intramuscularly) 3 h before the start of the scan. Propofol (6 mg/kg/h) and vecuronium (0.02 mg/kg/h) was also infused continuously. For the inhibition of the peripheral metabolism of [^{18}F]FDOPA, carbidopa [5 mg/kg, i. v. (Chan et al., 1995; Cumming and Gjedde, 1998)] was administered 1 h before the injection of [^{18}F]FDOPA. The study protocol was approved by the Subcommittee for Laboratory Animal Welfare of the National Cardiovascular Center.

Scanning procedure

A PET scan was performed by PCA-2000A positron scanner (Toshiba Medical Systems Corporation, Tochigi, Japan. Spatial resolution: 6.2 mm, axial FOV: 162 mm), which was manufactured by OEM of Siemens ECAT ACCEL (Herzog et al., 2004). A transmission scan with a 3-rod source of ^{68}Ge-^{68}Ga was carried out for 15 min for attenuation correction 1 h before the [^{18}F]FDOPA injection. A 2D dynamic emission scan of 120 min duration with 45 frames (10 s × 18, 30 s × 6, 120 s × 7, 300 s × 8, 600 s × 6 frames), was initiated upon intravenous injection of [^{18}F]FDOPA (102 MBq).

Data processing

Data were corrected for scattered and attenuated photons and reconstructed by 2D direct-inversion Fourier transform (DIFT) algorithm (Herzog et al., 2004; Stark et al., 1981) with 3 mm FWHM Gaussian filter. ROIs were defined manually over the striatum and cerebellum for PET images, and TAC in these regions were obtained.

Acquisition for input function

For continuous measurement of the arterial input function, the radioactivity in the artery was measured by γ ray detector with GSO crystal (Kudomi et al., 2003) and a shunt line inserted between the artery and vein of the monkey. In addition, the arterial blood was sampled at 3, 10, 30, 60, 120 min after injection of [^{18}F]FDOPA for the correction of radiotracer in hemocyte and radiolabeled metabolites. The radioactivity of whole blood and supernatant of the centrifuged samples were measured by well counter (BeWell QS01A, Molecular Imaging Laboratory, Osaka, Japan) for acquisition of whole blood and plasma radioactivity, 0.6 ml of supernatant of sample at 10, 60, and 120 min was deproteinized as described previously (Cumming et al., 1999). The fraction for [^{18}F]FDOPA and [^{18}F]OMFD in these supernatants were measured with high-performance liquid chromatography (HPLC) with a C-18 reverse phase column and a flow through γ detector(BeWell QS01B, Molecular Imaging Laboratory, Osaka, Japan).

The arterial input function obtained by continuous measurement was corrected for the plasma fraction. Input functions for [^{18}F]FDOPA and [^{18}F]OMFD were calculated from plasma activity and fraction for radiolabeled metabolite with bi-exponential function (Takikawa et al., 1994), derived from the [^{18}F]FDOPA fraction measured by HPLC.

Simulation for TAC

In all simulations by DF model, total radioactivity was calculated by solving the differential equations using a four-dimensional Runge-Kutta algorithm as previous study (Matsubara et al., 2010). The definition of kinetic terms and concentration in the following equation is described in Table II. K_1^M and k_2^M, estimated by compartmental model analysis in cerebellum TAC as described in the previous study (Kumakura et al., 2005), were given in TAC simulation. For definition of K_1^D, k_2^D, k_3, and V_b, compartmental analysis with the model including k_{loss} (Wahl and Nahmias, 1996) was applied to a monkey striatal

TABLE II. Definitions of kinetic term in DF model

Terms	Units	Definition
K_1	g/ml/min	Rate constant for influx of tracer to tissue across Blood-Brain Barrier (BBB). K_1^D for FDOPA and K_1^M for OMFD.
k_2	min^{-1}	Rate constant for diffusion of tracer from tissue to plasma. k_2^D for FDOPA and k_2^M for OMFD.
k_3	min^{-1}	Rate constant for the activity of DOPA decarboxylase, the enzyme for the decarboxylation from FDOPA to FDA.
k_5	min^{-1}	Rate constant for the activity of catechol-*O*-methyltransferase for the catabolism from FDOPA to OMFD.
k_7	min^{-1}	Rate constant for dopamine storage to the vesicle.
k_8	min^{-1}	Rate constant for recycle to cytosolic FDA.
k_9	min^{-1}	Rate constant for metabolism to the acidic metabolites. k_9^{dopac} for FDA to FDOPAC and k_9^{hva} for FDOPAC to FHVA.
k_{11}	min^{-1}	Rate constant for diffusion of the acidic metabolites. k_{11}^{dopac} for FDOPAC and k_{11}^{hva} for FHVA.
V_b	g/ml	Effective blood volume.

TABLE III. Rate constants given in simulation for normal condition

Parameter	Value	Parameter	Value	Parameter	Value
K_1^D	0.0202[a]	k_5	0.000[d]	k_{11}^{dopac}	0.0370[c]
k_2^D	0.0375[a]	k_7	0.0300[c]	k_{11}^{hva}	0.0370[c]
K_1^M	0.0156[b]	k_8	0.0200[c]	V_b	0.0408[a]
k_2^M	0.0391[b]	k_9^{dopac}	0.0170[c]		
k_3	0.0500[a]	k_9^{hva}	0.0272[c]		

Units: g/ml/min (K_1^D, K_1^M), g/ml (V_b), min^{-1} (other parameters).
[a]Values estimated by compartment analysis of monkey striatal TAC [model: two-tissue-four parameters model (Wahl and Nahmias, 1996)].
[b]Values estimated by compartment analysis of monkey cerebellar TAC as well as the previous report (Kumakura et al., 2005).
[c]Values close to the reported value (Cumming and Gjedde, 1998; Cumming et al., 1994; Deep et al., 1997).
[d]We regarded this parameter as negligible as well as the previous studies (Ishikawa et al., 1996; Wahl and Nahmias, 1996).

TAC, which is corrected by tissue OMFD TAC calculated from estimated K_1^M and k_2^M.

k_7 and k_8, which are in the range determined by the previous rat study (Deep et al., 1997), were given, such that simulated standard TAC corresponds to a measured TAC in monkey striatum. Values estimated in ex vivo rat study (Cumming et al., 1994) were given as k_9^{dopac}, k_9^{hva}, k_{11}^{dopac}, k_{11}^{hva}. k_5 were set to zero in simulation.

Values of rate constants given in simulation of the standard TAC are shown in Table III. For the case of the decrease in DDC activity, k_3 was altered between 0.0000 and 0.0500 min^{-1} (between −100 and 0% to the value in Table III). In simulation of the reduction in dopamine storage, k_7 was changed between 0.0000 and 0.0300 min^{-1} (between −100 and 0% to the value in Table III). Similarly, in simulation of the increase in dopamine metabolism to DOPAC, k_9^{dopac} was changed between 0.0170 and 0.0340 min^{-1} (between 0 and +100% to the value in Table III).

Calculation of noisy TACs

Standard deviation (SD) on PET count data in a voxel is in proportion to the inverse of root of noise equivalent count (NEC) as the following equation (Pajevic et al., 1998; Shidahara et al., 2008; Watabe et al., 2000):

$$\frac{\sigma}{C} = \alpha \cdot \frac{1}{\sqrt{NEC}} \quad (1)$$

where σ is SD on PET count data, C is count in PET image, and α is constant which depends on γ-ray scatter and dead time of detector. α value of PET scanner used in this study was pre-calculated cylinder phantom data (α = 14203.3). NEC data were obtained from actual PET study with a monkey described above. We generated 100 replications of TACs including voxel-level noise from noise-free TACs simulated.

Correction for OMFD

[^{18}F]3-*O*-methyl-FDOPA ([^{18}F]OMFD), the peripheral metabolite of [^{18}F]FDOPA, can cross the blood-brain barrier (BBB) and penetrate the brain tissue. Because [^{18}F]OMFD affects the kinetic analysis, it is necessary to remove [^{18}F]OMFD component from the tissue time-activity curve. The previous analyses (Holden et al., 1997; Martin et al., 1989; Sossi et al., 2001), have assumed uniform diffusion of [^{18}F]OMFD throughout the brain (Doudet et al., 1991), and the contribution of [^{18}F]OMFD was corrected via subtraction of the cerebellum activity from that in a region of interest (e.g., striatum). Note that the cerebellum is taken to be a reference region in which specific binding of [^{18}F]FDOPA is negligible. However, it is acknowledged that the subtraction of the reference region results in overcorrection for [^{18}F]OMFD because some of the reference region activity is attributed to [^{18}F]FDOPA (Kumakura et al., 2005, 2007). To avoid this overcorrection, the [^{18}F]OMFD component in the striatum were calculated from the parameters estimated by compartment analysis of the cerebellar TAC (Kumakura et al., 2005, 2006, 2007).

OMFD component in the simulated TACs were calculated by the following equation, and corrected in all analyses of this study except for Gjedde-Patlak analysis.

$$C_{OMFD}(t) = K_1^M \int_0^t C_a^M(\tau) e^{-k_2^M}(t-\tau) d\tau \quad (2)$$

K_1^M and k_2^M values estimated from cerebellum TAC as described above. Then, simulated total tissue TACs were corrected by calculated OMFD component. For K_i estimation by Gjedde-Patlak method, OMFD com-

ponent in TACs were corrected via subtraction of the cerebellar TAC in monkey as described previously (Martin et al., 1989).

Data analysis and evaluation of sensitivity

For the Gjedde-Patlak and Logan methods, linear regression analysis proceeded following Eqs. 3 and 4, respectively.

$$\frac{\bar{C}_{\mathrm{PET}}(t)}{C_{\mathrm{a}}^{\mathrm{D}}(t)} = K_{\mathrm{i}} \cdot \frac{\int_0^t C_{\mathrm{a}}^{\mathrm{D}}(\tau)d\tau}{C_{\mathrm{a}}^{\mathrm{D}}(t)} + \text{inter sept} \quad (3)$$

$$\frac{\int_0^t \bar{C}_{\mathrm{PET}}(\tau)d\tau}{C_{\mathrm{PET}}(t)} = V_{\mathrm{T}} \cdot \frac{\int_0^t C_{\mathrm{a}}^{\mathrm{D}}(\tau)d\tau}{C_{\mathrm{PET}}(t)} + \text{inter sept} \quad (4)$$

C_{PET} is defined as total radioactivity minus the OMFD contribution (units: Bq/ml). K_{i} and V_{T} were estimated from the slope in linear regression. In the analysis implementing the Kumakura method, Eq. 5 was used for multilinear regression.

$$\int_0^t \bar{C}_{\mathrm{PET}}(\tau)d\tau = V_{\mathrm{T}} \cdot \int_0^t C_{\mathrm{a}}^{\mathrm{D}}(\tau)d\tau - \frac{\bar{C}_{\mathrm{PET}}(t)}{k_{\mathrm{loss}}} + \frac{V_{\mathrm{f}} + V_{\mathrm{b}}}{k_{\mathrm{loss}}} \cdot C_{\mathrm{a}}^{\mathrm{D}}(t) \quad (5)$$

Three coefficients, V_{T}, $1/k_{\mathrm{loss}}$, $(V_{\mathrm{f}}+V_{\mathrm{b}})/k_{\mathrm{loss}}$, were estimated by multilinear regression. For this analysis, 60–120 min TAC data were employed.

To compare the sensitivity of macro parameters to simulated alterations in [^{18}F]FDOPA kinetics, the percentage difference between macro parameters estimated from TACs with altered k_3, k_7, or k_9^{dopac}, were compared to the same macro parameters estimated from the standard TAC. The percent change was calculated by the following equation.

$$\%\text{change} = \frac{p - p_{\mathrm{std}}}{p_{\mathrm{std}}} \times 100 \quad (6)$$

p and p_{std} were defined as values of parameters estimated from TAC in case of altering k_3, k_7, or k_9^{dopac} and standard TAC, respectively. We regarded %change as the sensitivity to changes in each pathway.

To confirm whether macro parameters can detect the alteration with k_3, k_7, or k_9^{dopac} in noisy case, we examined Welch's t test between macro parameters estimated from altered TACs and standard TACs.

RESULTS

A standard TAC simulated by given rate constants in Table III and metabolite-corrected input functions are shown in Figure 3. The simulated standard TAC nearly corresponded to the measured TAC. TACs in the case of altering k_3, k_7, or k_9^{dopac} are shown in Figure 4. The smaller the k_7 value was, the more rapidly

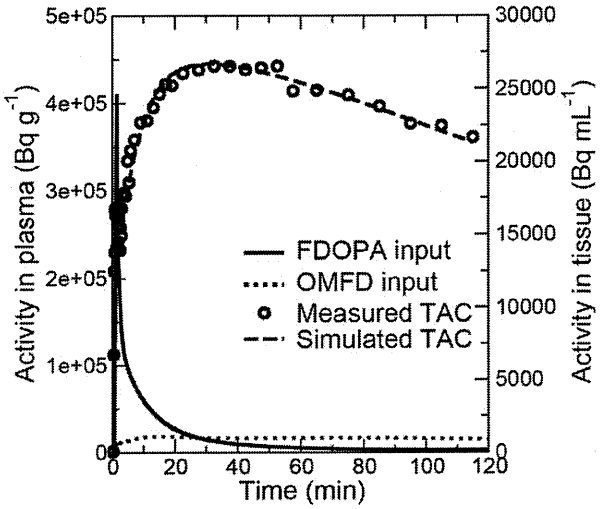

Fig. 3. Input functions and standard TAC as normal condition.

the TAC declined after 50 min post-injection of [^{18}F]FDOPA. Similarly, in the case of increased k_9^{dopac}, a greater reduction of the TAC was observed after 30 min post-injection.

In most of the regression by three conventional methods in both noise-free and noise-added cases, good correlations were observed (correlation coefficients r were $\geq$0.71, $\geq$0.77, and $\geq$0.99 for Gjedde-Patlak, Logan, and Kumakura method, respectively). However, some regression by Gjedde-Patlak analysis to voxel-level noise added data were failed.

Trends of %change calculated from parameters estimated by three methods are shown in Figure 5. In noise-free evaluation, k_{loss} estimated by Kumakura method showed the largest %change to changes in k_7 and k_9^{dopac}. The other macro parameters also change moderately with the changes in k_7 and k_9^{dopac}. For the case of decreasing k_3 from 0.0500 to 0.0100 min^{-1}, the %change of K_{i} and V_{T} were greater than k_{loss}. However, when k_3 was approximately zero, k_{loss} increased quite dramatically.

Addition of voxel-level noise caused large variation and bias of k_{loss}. The changes in k_{loss} estimated from voxel-level noise added data to k_3, k_7 or k_9^{dopac} were not significant ($P > 0.05$), except for the case $k_3 < 0.0250$ min^{-1}. K_{i} and V_{T} were not affected by voxel-level noise. These two parameters changed significantly to the alteration of k_3, k_7, or k_9^{dopac} ($P < 0.05$).

DISCUSSION

Our study aimed to compare the sensitivity of conventional macro parameters to the changes of DDC activity, dopamine storage in the vesicle, and dopamine metabolism to the acidic metabolites. We developed the model with detailed pathways in the dopa-

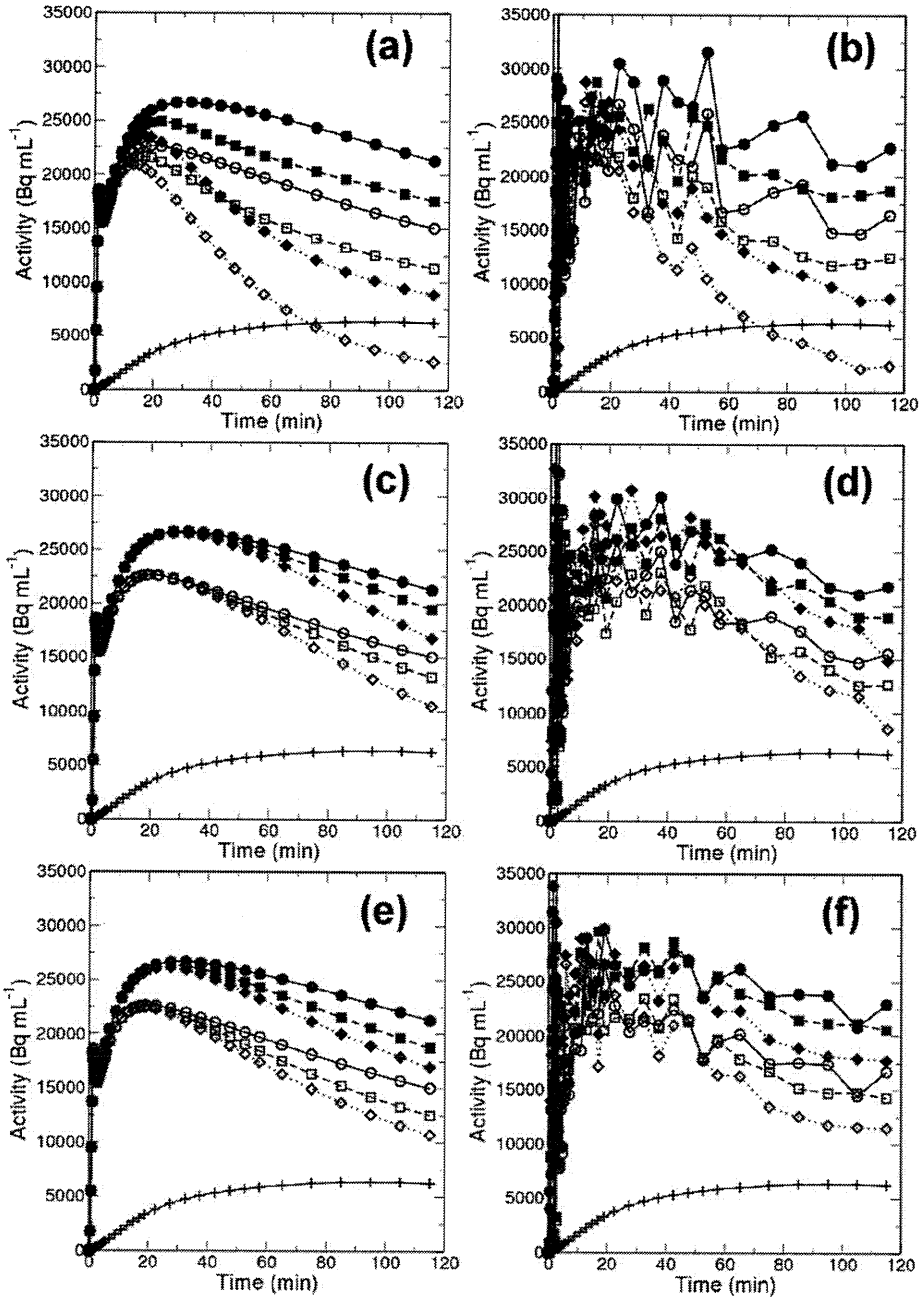

Fig. 4. Simulated TACs in the case of altering k_3 [upper row: (a), (b)], k_7 [middle row: (c), (d)], or k_9^{dopac} [bottom row: (e), (f)]. Noise free or noise added TACs were shown in left column [(a), (c), and (e)] or right column [(b), (d), and (f)], respectively. Legends: closed symbols: simulated TACs, open symbols: TACs corrected for OMFD component, plus symbols: OMFD TACs, solid lines: standard TACs, dashed lines: TACs in case to alter the rate constant by -50% (k_3, k_7) or $+50\%$ (k_9^{dopac}), dotted lines: TACs in case to alter the rate constant by -100% (k_3, k_7) or $+100\%$ (k_9^{dopac}).

mine neuron (DF model) and simulated TACs with changes in DDC activity (k_3), dopamine storage in the vesicle (k_7), and metabolism from dopamine to DOPAC (k_9^{dopac}). Three macro parameters, the net influx of FDOPA (K_i), total distribution volume (V_T), and the rate constants for clearance of the acidic metabolites of FDA from the tissue, k_{loss}, were estimated by three conventional methods with linear least squares algorithm, Gjedde-Patlak graphical analysis (Gjedde, 1981, 1982; Martin et al., 1989; Patlak and Blasberg, 1985; Patlak et al., 1983), Logan graphical analysis, which is popular method in recep-